UC San Diego
UC San Diego Previously Published Works

Title

Mitochondrial morphology governs ATP production rate.

Permalink

Journal

Authors

Garcia, Guadalupe

Gupta, Kavya

Bartol, Thomas

et al.

Publication Date

DOI

Peer reviewed

ARTICLE

Mitochondrial morphology governs ATP production rate

Guadalupe C. Garcia[1] , Kavya Gupta[2] , Thomas M. Bartol[1] , Terrence J. Sejnowski[1] , and Padmini Rangamani[2]

Life is based on energy conversion. In particular, in the nervous system, significant amounts of energy are needed to maintain synaptic transmission and homeostasis. To a large extent, neurons depend on oxidative phosphorylation in mitochondria to meet their high energy demand. For a comprehensive understanding of the metabolic demands in neuronal signaling, accurate models of ATP production in mitochondria are required. Here, we present a thermodynamically consistent model of ATP production in mitochondria based on previous work. The significant improvement of the model is that the reaction rate constants are set such that detailed balance is satisfied. Moreover, using thermodynamic considerations, the dependence of the reaction rate constants on membrane potential, pH, and substrate concentrations are explicitly provided. These constraints assure that the model is physically plausible. Furthermore, we explore different parameter regimes to understand in which conditions ATP production or its export are the limiting steps in making ATP available in the cytosol. The outcomes reveal that, under the conditions used in our simulations, ATP production is the limiting step and not its export. Finally, we performed spatial simulations with nine 3-D realistic mitochondrial reconstructions and linked the ATP production rate in the cytosol with morphological features of the organelles.

Introduction

Energy conversion is at the core of cellular function. Finding efficient strategies to transduce energy has driven the evolution of cells and organisms. In eukaryotic cells, respiration occurs in specialized organelles known as mitochondria. There, metabolic substrates are converted to adenosine triphosphate (ATP), the energy currency of the cell (Alberts et al., 2015). Mitochondrial architecture provides an efficient framework for cellular respiration. It is composed of two distinct membranes: the outer membrane (OM) and the inner membrane (IM). The IM is used to generate an electrochemical proton gradient through a series of electron carriers known as the electron-transport chain (ETC; Fig. 1). The energy stored in this gradient drives the synthesis of ATP from adenosine diphosphate (ADP) and inorganic phosphate (Pi) through a multiprotein complex, ATP synthase (Yoshida et al., 2001). The outer membrane plays a central role in controlling the flow of molecules from and to the interior of mitochondria. Although it forms a barrier to large molecules, it contains a large number of proteins, voltage-dependent anion channels (VDAC; Colombini, 2004), that allow the passage of small metabolites and ions. In contrast, the IM is impermeable to molecules; carrier proteins

and ion channels are required for molecules to cross this barrier. One of the most relevant carriers is the adenine nucleotide translocator (ANT), which transports ATP and ADP to and from the matrix, the internal region encapsulated by the IM (Fig. 1). Overall, this is a membrane-based process that relies on the lipid bilayer of mitochondria to generate the energy required for ATP synthesis.

The importance of ATP production by mitochondria means that reliable mathematical formulations are necessary to build a quantitative framework. To that effect, there have been many mathematical models developed to describe the processes involved in ATP production (Pietrobon and Caplan, 1985; Magnus and Keizer, 1997; Cortassa et al., 2003; Nguyen et al., 2007; Bertram et al., 2006; Beard, 2005; Heiske et al., 2017; Garcia et al., 2019). Pietrobon and Caplan (1985) developed a proton pump model that can be interpreted as a respiration-driven proton pump or as a model of ATP synthase (Magnus and Keizer, 1997). Later on, Magnus and Keizer (1997) assembled different components and built a steady-state model of ATP production in mitochondria, which several other models are based on (Cortassa et al., 2003; Bertram et al., 2006; Nguyen

---

[1]Computational Neurobiology Laboratory, Salk Institute for Biological Studies, La Jolla, CA, USA; [2]Department of Mechanical and Aerospace Engineering, University of California, San Diego, La Jolla, CA, USA.

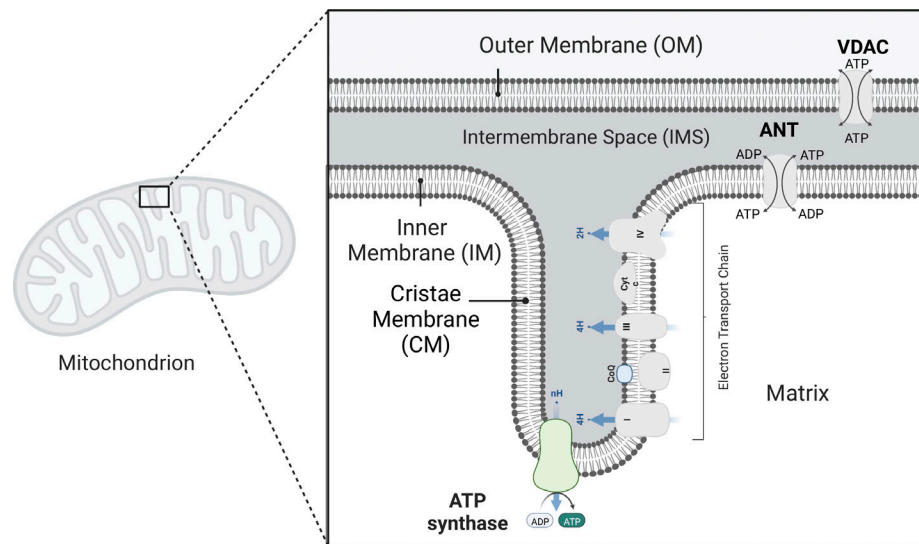Correspondence to Padmini Rangamani: prangamani@ucsd.edu

Figure 1. **Schematic representation of a mitochondrion with its functional components and compartments.** The OM is the external lipid bilayer that interfaces with the cytosol. The IM encapsulates the matrix and is composed of two functionally distinct regions, the inner boundary membrane (IBM; in close opposition to the OM) and the CM. The CM is the place where the protein complexes from the electron-transport chain (ETC) reside. At the apex of the CM and along the tubular cristae, ATP synthases are allocated. Through these protein complexes, ATP is synthesized in the matrix. ATP is further transported from the matrix through ANTs to the intermembrane space (IMS)—the space between the two membranes—to finally cross the OM at the VDAC into the cytosol.

et al., 2007). However, they did not explicitly show how the thermodynamic constraints were imposed on the system[1]. Some of these models also have been built to be consistent with thermodynamic laws (Beard, 2005; Heiske et al., 2017), and in most cases include more components as the activity of the TCA cycle (Cortassa et al., 2003; Nguyen et al., 2007) enzymes or the activity of other components of the ETC (Beard, 2005; Heiske et al., 2017). Almost all previously developed models are implemented with ordinary differential equations (ODEs), disregarding the spatial organization of mitochondria. Here and in our previous work (Garcia et al., 2019), our efforts were focused on developing a minimal reaction-based mitochondrion model so that we can implement it to perform spatial simulations in MCell (Stiles et al., 1996; Kerr et al., 2008; Husar et al., 2022 *Preprint*) or non-spatial simulations. In this work, we ensure the model is thermodynamically consistent, and for that we imposed detailed balance constraints to the reaction rate constants.

With the model developed here, we answered the following questions: under physiological conditions, what limits the amount of ATP that reaches the cytosol? Is it the rate of ATP production or is it the rate of ATP export from the mitochondria to the cytosol? To answer these questions, we developed a thermodynamically consistent model of ATP production in mitochondria—i.e., a physically plausible model. Our criteria for thermodynamic consistency was to calculate thermodynamic forces (Hill, 1989) for each cycle in the model and to equate them to the ratio of the forward-to-backward reaction rate constants. In this manner, we verified that detailed balance is satisfied for the conditions considered. Furthermore, we calculated the dependence of the reaction rate constants on the membrane

potential, pH, ATP, ADP, and Pi concentrations. We conducted simulations of this model using ODEs; although simpler, this approach is informed with detailed structural calculations of surface areas and volumes from a realistic 3-D reconstruction (Garcia et al., 2019). The outcomes reveal that, under physiological conditions, ATP production in the matrix is the limiting factor. Lastly, we used the model to perform spatial simulations using nine realistic 3-D reconstructions (Mendelsohn et al., 2021). Our results link the ATP production rate to structural features of the mitochondrial geometries.

Materials and methods
The model presented here is based on previous work (Pietrobon and Caplan, 1985; Magnus and Keizer, 1997; Metelkin et al., 2006; Garcia et al., 2019). Our efforts were focused on assembling a thermodynamically consistent model (Hill, 1989) and explicitly highlighting the dependence of the reaction rate constants on the membrane potential, pH, ATP, ADP, and Pi concentration.

Model for ATP synthase
The ATP synthase model is grounded on the work of Pietrobon and Caplan (1985). The kinetic model consists of a membrane protein—represented as E—that transports protons (H^{+}) from the intermembrane space (IMS) to the matrix. The protein can be in six states, represented in Fig. 2 A. Each state is associated with a number from 1 to 6 (Fig. 2 B). A clockwise cycle starting in state 6 (E[−3]) represents the binding of three protons from the IMS (transition 6 → 5 in Fig. 2 B), transport of the protons to the matrix (state 5 → 4), binding of ADP and Pi (state 4 → 3), and subsequent synthesis of ATP (state 3 → 2), followed by unbinding of the protons in the matrix (state 2 → 1). We considered a constant proton concentration inside the IMS and the matrix,
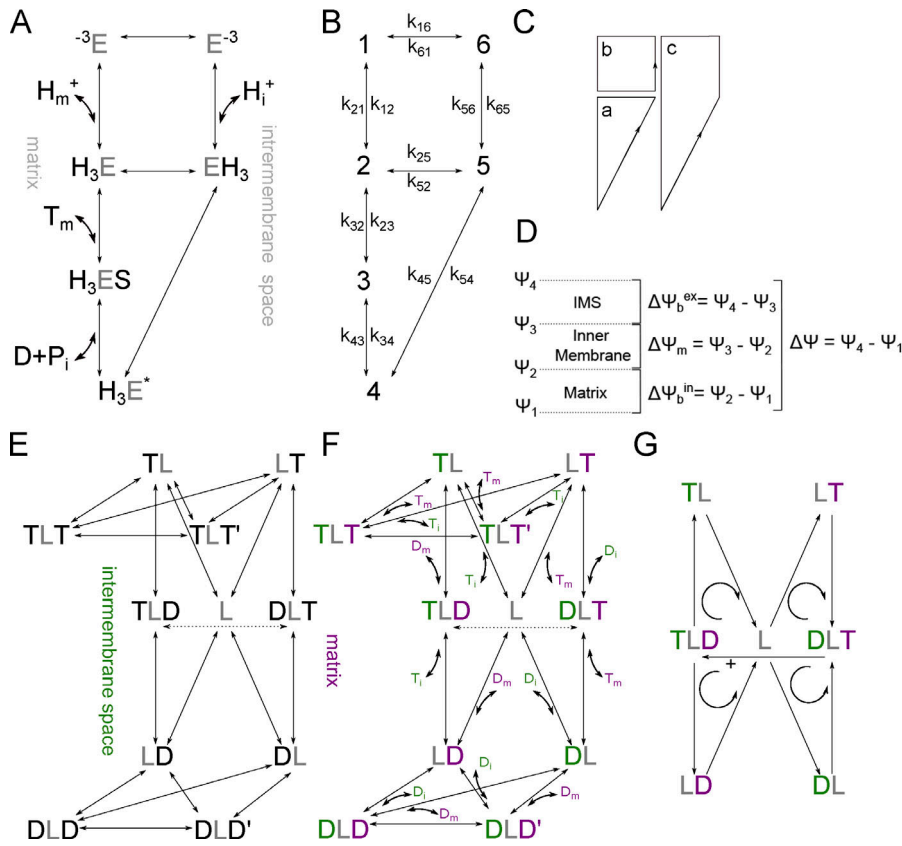
Figure 2. **Kinetic diagram of the modules of the mitochondria model. (A–C)** Kinetic diagram of the ATP synthase model (Pietrobon and Caplan, 1985). **(A)** The model consists of six states, representing different protein configurations. ATP molecules are represented as T, ADP molecules as D, phosphate as Pi, ATP synthase as E, and H⁺ as protons. The model considers the binding of ATP and ADP from the matrix and the IMS. **(B)** Each state is associated with a number from 1 to 6. A clockwise cycle, starting from state 6 corresponds to the binding of three protons from the IMS (6 → 5), followed by their transport to the matrix (5 → 4) and subsequent binding of ADP and Pi (4 → 3), to the synthesis of ATP (3 → 2), and unbinding of three protons in the matrix (2 → 1). Each transition has an associated rate constant k_{ij}. The list of all the reactions is in Table 1 and the list of parameters is in Table 2. **(C)** The cycles are considered positive in the counterclockwise direction and named a, b, and c. **(D)** Membrane potential considered in the ATP synthase model. $\Delta\Psi = \Psi_4 - \Psi_1$ is the electrical potential difference between the matrix and IMS (or cytosol), $\Delta\Psi_m$ is the electrical potential difference across the membrane, $\Delta\Psi_b^{in}$ and $\Delta\Psi_b^{ex}$ are the phase-boundary potentials. **(E–G)** Kinetic diagram of the ANT model. **(E)** The model consists of 11 states, L represents the free protein, and YLX is a triple molecular state with one X molecule bound from the matrix side and one Y molecule bound from the IMS. X and Y represent ATP or ADP molecules, respectively. The model has been adapted from previous work (Metelkin et al., 2006). **(F)** In this representation, the binding and unbinding of ATP and ADP are explicitly shown, molecules from the IMS side are in green, and those from the matrix side are in purple. **(G)** The cycles are considered positive going from the matrix to the IMS.

and the ATP and ADP concentration as variables. The list of the reactions is given in Table 1, and the model parameters are given in Tables 2. The number of ATP synthases used in the model was determined employing the density estimated at 3,070 μm⁻² (Acehan et al., 2011). Given the surface area of high curvature of the IM in the reconstructions (Mendelsohn et al., 2021), we estimated the number of ATP synthases as 267 for mitochondrial reconstruction #1 (Mito 1).

Table 1. **List of reactions for the ATP synthase model**

List of reactions for the ATP synthase model
$^{-3}E + 3H_m^+ \underset{k_{21}}{\overset{k_{12}}{\rightleftharpoons}} H_3E$
$H_3E + T_m^+ \underset{k_{32}}{\overset{k_{23}}{\rightleftharpoons}} k_{23}H_3ES$
$H_3ES \underset{k_{43}}{\overset{k_{34}}{\rightleftharpoons}} k_{34}H_3E^* + D_m$
$H_3E^* \underset{k_{54}}{\overset{k_{45}}{\rightleftharpoons}} k_{45}EH_3$
$EH_3 \underset{k_{65}}{\overset{k_{56}}{\rightleftharpoons}} k_{56}E^{-3} + H_i^+$
$E^{-3} \underset{k_{16}}{\overset{k_{61}}{\rightleftharpoons}} {}^{-3}E$

We next explain how some kinetic parameters depend on the membrane potential, the proton concentration, and the phosphate concentration.

Thermodynamic constraints

Thermodynamic constraints are imposed on the rate constants of the system. At an arbitrary steady-state, the product of the first-order (or pseudo-first-order) rate constants around a cycle κ in the positive direction ($\prod_{k+}$) divided by the product of the rate constants in the negative direction ($\prod_{k-}$) is related to net thermodynamic forces in the following manner (Hill, 1989):

$$\frac{\prod_{k+}}{\prod_{k-}} = e^{\left(\frac{\chi}{RT}\right)} = e^{\left(\frac{\Delta G_\kappa}{RT}\right)}, \qquad (1)$$

where χ is the net thermodynamic force, ΔG_κ is the difference in Gibbs free energy per mole of a substance (i.e., the chemical potential) in the cycle κ, R is the universal gas constant, and T is the absolute temperature. At thermodynamic equilibrium, and in the absence of a potential difference between the membranes, the ΔG in the cycle is zero. This leads to a ratio of forward rate constants to backward rate constants equal to one (Eq. 1), also known as detailed balance.

Table 2. **Parameters for the ATP synthase model**

Parameter	Definition	Value	Unit	Reference
F	Faraday's constant	9.649×10^4	$C\,mol^{-1}$	Keener and Sneyd (1998)
R	Universal gas constant	8.315	$J\,mol^{-1}\,K^{-1}$	Keener and Sneyd (1998)
pH_m	Matrix pH	7.6		Magnus and Keizer (1997)
pH_c	Cristae pH	7.2		Magnus and Keizer (1997)
[Pi]	Phosphate concentration	20	mM	Pietrobon and Caplan (1985)
T	Temperature	310	K	
K	Equilibrium constant	1.71×10^6	M	Pietrobon and Caplan (1985)
$\Delta\psi$	Membrane potential	180	mV	Holmuhamedov et al. (1998)
$\Delta\psi_{B,i}$	Phase boundary potential	−50	mV	Pietrobon and Caplan (1985)
$\Delta\psi_{B,M}$	Phase boundary potential	0	mV	Pietrobon and Caplan (1985)
$k_{61,0}$	Rate constant at 0 mV	4.98×10^7	s^{-1}	Pietrobon and Caplan (1985)
$k_{16,0}$	Rate constant at 0 mV	1×10^2	s^{-1}	Pietrobon and Caplan (1985)
$k_{56,0}$	Rate constant at 0 mV	2.75×10^5	s^{-1}	Pietrobon and Caplan (1985)
$k_{21,0}$	Rate constant at 0 mV	40	s^{-1}	Pietrobon and Caplan (1985)
k_{43}^*	Rate constant[b]	1×10^8	$M^{-2}\,s^{-1}$	Pietrobon and Caplan (1985)
k_{12}^*	Rate constant[b]	6.33×10^{24}	$M^{-3}\,s^{-1}$	Pietrobon and Caplan (1985)
k_{65}^*	Rate constant[b]	1.58×10^{25}	$M^{-3}\,s^{-1}$	Pietrobon and Caplan (1985)
k_{23}^*	Rate constant[b]	5×10^6	$M^{-1}\,s^{-1}$	Pietrobon and Caplan (1985)
k_{54}	Rate constant	1×10^2	s^{-1}	Pietrobon and Caplan (1985)
k_{32}	Rate constant	5×10^3	s^{-1}	Pietrobon and Caplan (1985)
k_{34}	Rate constant	100	s^{-1}	Pietrobon and Caplan (1985)
k_{45}	Rate constant	100	s^{-1}	Pietrobon and Caplan (1985)
k_{56}	Rate constant	1,000	s^{-1}	Pietrobon and Caplan (1985)
k_{25}	Rate constant	5.85×10^{-30}	s^{-1}	Pietrobon and Caplan (1985)
k_{52}	Rate constant	1×10^{-20}	s^{-1}	Pietrobon and Caplan (1985)
k_{43}	Rate constant[c]	2×10^6	$M^{-1}\,s^{-1}$	Pietrobon and Caplan (1985)
k_{12}	Rate constant[c]	25	s^{-1}	Pietrobon and Caplan (1985)
k_{65}	Rate constant[c]	3,969	s^{-1}	Pietrobon and Caplan (1985)
k_{61}	Rate constant at 180 mV	33,989	s^{-1}	Pietrobon and Caplan (1985)
k_{16}	Rate constant at 180 mV	146,516	s^{-1}	Pietrobon and Caplan (1985)
k_{56}	Rate constant at 180 mV	1,000	s^{-1}	Pietrobon and Caplan (1985)
k_{21}	Rate constant at 180 mV	40	s^{-1}	Pietrobon and Caplan (1985)
δ_{atp}	Density of ATP synthases	3,070	μm^{-2}	Acehan et al. (2011)
$\#ATP_{syn1}$	Number of ATP synthases for Mito #1	267		[a]

[a]Our estimation, given the surface area of high curvature of the IM measured in the reconstruction (Mendelsohn et al., 2021).
[b]Independent of the concentration.
[c]Concentration dependent.

Starting with the shortest cycle, b in Fig. 2 C, we obtain

$$\frac{\prod_b+}{\prod_b-} = e^{\left(\frac{\chi}{RT}\right)} = e^{\left(\frac{\Delta G_b}{RT}\right)}. \qquad (2)$$

Replacing the rate constants in the cycle we get

$$\frac{k_{12}k_{25}k_{56}k_{61}}{k_{21}k_{52}k_{65}k_{16}} = K_{12}K_{25}K_{56}K_{61}, \qquad (3)$$

where K_{ij} are the equilibrium constants of the transitions from state i to state j. The equilibrium constants are given by Caplan and Essig (1983),

$$K_{ij} = \frac{k_{ij}}{k_{ji}} = e^{\frac{G_i - G_j}{RT}}, \tag{4}$$

where G_i and G_j are the Gibbs free energy per mole for species in states i and j, respectively. The equilibrium constant for the transition from state 1 to 2, where three protons bind from the matrix side, is equal to:

$$K_{12} = \frac{k_{12}}{k_{21}} = e^{\frac{G_1 - G_2}{RT}}, \tag{5}$$

where G_1 is the Gibbs free energy per mole of three protons in the matrix and G_2 is the energy of the protons bound to the membrane. These are given by Caplan and Essig (1983),

$$G_1 = G_1^o + 3F\psi_1 + 3RT\ln([H_m^+]), \quad G_2 = G_2^o + 3F\psi_2, \tag{6}$$

where G_1^o and G_2^o are the standard free energy per mole. Here, Ψ_1 is the bulk potential at the matrix, Ψ_2 is the phase boundary potential at the surface of the inner membrane (Fig. 2 D), and F is the Faraday's constant. Replacing Eq. 6 in Eq. 5 we arrive at

$$\frac{k_{12}}{k_{21}} = e^{\left(\frac{G_1^o - G_2^o}{RT}\right)} e^{\left(\frac{-3F\Delta\Psi_b^{in}}{RT}\right)} [H_m^+]^3, \tag{7}$$

where $\Delta\Psi_b^{in} = \Psi_2 - \Psi_1$ is the phase-boundary potential (the difference between the bulk potential and the potential at the surface of the membrane; see Fig. 2 D) and $[H_m^+]$ is the proton concentration in the matrix. We define $k_{ij,0}$ as the rate constant at zero potential difference and k_{ij}^* as the rate constant independent of the concentrations, and we arrive at:

$$\frac{k_{12}}{k_{21}} = \frac{k_{12}^*}{k_{21,0}} e^{\left(\frac{-3F\Delta\Psi_b^{in}}{RT}\right)} [H_m^+]^3. \tag{8}$$

Following the original model (Pietrobon and Caplan, 1985), we assign the effect of the phase-boundary potentials to the unbinding rate constant k_{21} and proton concentration to the binding rate constant k_{12}:

$$k_{21} = k_{21,0} e^{\left(\frac{3F\Delta\Psi_b^{in}}{RT}\right)}, \quad k_{12} = k_{12}^* [H_m^+]^3. \tag{9}$$

We take a similar approach for the transition $6 \rightarrow 5$, where three protons bind from the IMS to the IM. The Gibbs energy per mole for the protons in the IMS (G_6) and bound to the membrane (G_5) are:

$$G_6 = G_6^o + 3F\Psi_4 + 3RT\ln([H_i^+]), \quad G_5 = G_5^o + 3F\Psi_3. \tag{10}$$

Replacing Eq. 10 in Eq. 4 we arrive at:

$$K_{65} = \frac{k_{65}}{k_{56}} = e^{\left(\frac{G_6^o - G_5^o}{RT}\right)} e^{\left(\frac{-3F\Delta\Psi_b^{ex}}{RT}\right)} [H_i^+]^3, \tag{11}$$

where $\Delta\Psi_b^{ex} = \Psi_4 - \Psi_3$ is the phase-boundary potential from the IMS and H_i^+ is the proton concentration in the IMS.

As before, we can rewrite Eq. 11 with the rate constant at zero potential difference and the rate constant independent of the concentration as:

$$\frac{k_{65}}{k_{56}} = \frac{k_{65}^*}{k_{56,0}} e^{\left(\frac{-3F\Delta\Psi_b^{ex}}{RT}\right)} [H_i^+]^3. \tag{12}$$

The effect of the phase-boundary potentials is assigned to the unbinding rate constants k_{56}, and the proton concentration to the binding rate constant k_{65}, and we obtain:

$$k_{56} = k_{56,0} e^{\left(\frac{3F\Delta\Psi_b^{ex}}{RT}\right)}, \quad k_{65} = k_{65}^* [H_i^+]^3. \tag{13}$$

The transition from state $1 \rightarrow 6$ involves the movement of the negatively charged proton binding site from the matrix to the IMS. Therefore, the Gibbs free energy for this transition can be written as

$$G_1 = G_1^o - 3F\Psi_2, \quad G_6 = G_6^o - 3F\Psi_3. \tag{14}$$

Here, Ψ_2 and Ψ_3 are the potentials at the respective membrane surfaces (Fig. 2). Replacing in Eq. 4 we arrive at:

$$K_{16} = \frac{k_{16}}{k_{61}} = e^{\left(\frac{G_1^o - G_6^o}{RT}\right)} e^{\left(\frac{3F\Delta\Psi_m}{RT}\right)}, \tag{15}$$

where $\Delta\Psi_m = \Psi_3 - \Psi_2$. As before, replacing with the rate constants at zero membrane potential difference we reach:

$$\frac{k_{16}}{k_{61}} = \frac{k_{16,0}}{k_{61,0}} e^{\left(\frac{3F\Delta\Psi_m}{RT}\right)}. \tag{16}$$

Following the original model (Pietrobon and Caplan, 1985), we considered a symmetrical Eyring barrier (Caplan, 1981). With this assumption, the individual rate constants can be written as:

$$k_{16} = k_{16,0} e^{\left(\frac{3F\Delta\Psi_m}{2RT}\right)}, \quad k_{61} = k_{61,0} e^{\left(\frac{-3F\Delta\Psi_m}{2RT}\right)}. \tag{17}$$

Substituting the equilibrium rate constants calculated above in Eq. 3 we arrive at:

$$\frac{k_{12}k_{25}k_{56}k_{61}}{k_{21}k_{52}k_{65}k_{16}} = \frac{k_{12}^*}{k_{21,0}} e^{\left(\frac{-3F\Delta\Psi_b^{in}}{RT}\right)} [H_m^+]^3 \frac{k_{25}}{k_{52}} \frac{k_{56,0}}{k_{65}^*} e^{\left(\frac{3F\Delta\Psi_b^{ex}}{RT}\right)}$$
$$[H_i^+]^{-3} \frac{k_{61,0}}{k_{16,0}} e^{\left(\frac{-3F\Delta\Psi_m}{RT}\right)}. \tag{18}$$

At thermodynamic equilibrium, detailed balance imposes an additional constraint on the rate constants:

$$\frac{k_{12}^* k_{25} k_{56,0} k_{61,0}}{k_{21,0} k_{52} k_{65}^* k_{16,0}} = 1, \tag{19}$$

which yields:

$$\frac{\Pi_b^+}{\Pi_b^-} = e^{\frac{-3F\left(\Delta\Psi_m - \Delta\Psi_b^{ex} + \Delta\Psi_b^{in}\right)}{RT}} \frac{[H_m^+]^3}{[H_i^+]^3} = e^{\left(\frac{-3F\Delta p}{RT}\right)}. \tag{20}$$

Here, Δp is the proton motive force:

$$\Delta p = \Delta\Psi - 2.303 \frac{RT}{F}\Delta pH, \tag{21}$$

where $\Delta\Psi$ is the total potential difference across the matrix and the IMS, and ΔpH is the pH difference across the IMS and the matrix ($\Delta pH = pH_i - pH_m$). Similarly, for cycle a (Fig. 2 C), we obtain

$$\frac{\prod_a +}{\prod_a -} = \frac{k_{23}k_{34}k_{45}k_{52}}{k_{32}k_{43}k_{54}k_{25}} = e^{\frac{\chi_a}{RT}}, \tag{22}$$

where χ_a is the thermodynamic force given by:

$$\chi_a = RT\ln\left(K\frac{[ATP]}{[ADP][Pi]}\right), \tag{23}$$

where K is the equilibrium constant of the ATP hydrolysis reaction. At equilibrium, we arrive at:

$$\frac{k_{23}k_{34}k_{45}k_{52}}{k_{32}k_{43}k_{54}k_{25}} = 1. \tag{24}$$

This yields:

$$\frac{k_{23}^{*}k_{34}k_{45}k_{52}}{k_{32}k_{43}^{*}k_{54}k_{25}} = K, \tag{25}$$

imposing further constraints on the rate constants. Finally, for the longest cycle c, the thermodynamic force is the sum of forces for cycles b and a:

$$\Delta G_c = \chi_a - 3F\Delta p$$
$$= RT\ln\left(K\frac{[ATP]}{[ADP][Pi]}\right) - 3F\left(\Delta\Psi - 2.303\frac{RT}{F}\Delta pH\right). \tag{26}$$

As before, the product of the reaction rate constants relates to the thermodynamic forces in the following manner:

$$\frac{\prod_c +}{\prod_c -} = \frac{k_{23}k_{34}k_{45}k_{52}}{k_{32}k_{43}k_{54}k_{25}} = e^{\frac{\chi_a}{RT}}e^{\frac{-3F\Delta p}{RT}}, \tag{27}$$

which at equilibrium can be expressed as:

$$\frac{k_{23}^{*}k_{34}k_{45}k_{52}}{k_{32}k_{43}^{*}k_{54}k_{25}} = Ke^{\frac{-3F\Delta p}{RT}}, \tag{28}$$

imposing further constraints on the rate constants.

We use the chemical reactions and rate constants presented above to implement the system using compartmental ODEs. As a result of our calculations, the system of ODEs for the ATP synthase model is given by:

$$\frac{dE^{-3}}{dt} = -k_{65}E^{-3} + k_{56}EH_3 + k_{16}^{-3}E - k_{61}E^{-3},$$
$$\frac{d^{-3}E}{dt} = -k_{16}^{-3}E + k_{61}E^{-3} - k_{12}^{-3}E + k_{21}H_3E,$$
$$\frac{dH_3E^{*}}{dt} = -k_{45}H_3E^{*} + k_{54}EH_3 + k_{34}H_3ES - k_{43}H_3E^{*}D_m,$$
$$\frac{dH_3ES}{dt} = k_{43}D_mH_3E^{*} - k_{34}H_3ES + K_{23}H_3ET_m - K_{32}H_3ES,$$
$$\frac{dH_3E}{dt} = -k_{23}H_3ET_m + k_{32}H_3ES - k_{25}H_3E + k_{52}EH_3 + k_{12}^{-3}E$$
$$\quad - k_{21}H_3E, \tag{29}$$

where variables E^{-3}, ^{-3}E, etc., are the number of molecules in the different states. The rate constants of the bimolecular reactions have been normalized to have proper units to compute the number of particles, i.e., $k = \frac{k'}{N_A V}$, where k′ represents the constants given in Table 2, N_A is the Avogadro's number, and V represents the volume. The volume is either the volume of the matrix or the IMS depending on where the specific reaction occurs (see Simulations methods). These five differential equations describe the dynamics of the ATP synthase model. The dynamics of the missing state EH_3 can be deduced since the total number of proteins is a conserved quantity (E_{tot}), leading to the conservation expression $E^{-3} + EH_3 + H_3E + H_3ES + H_3E^{*} + {}^{-3}E = E_{tot}$. E_{tot} is the total number of ATP synthases considered in the simulations, and this parameter is #ATP_{syn1} in Table 2.

Model for ATP/ADP translocator (ANT)

The ANT model is based on the work of Metelkin et al. (2006). It is composed of 11 states and 20 bidirectional transitions. The kinetic diagram is shown in Fig. 2 F. The free protein (L) can bind molecules from the matrix (on the right) or IMS side (on the left), forming a triple molecular state (YLX), where Y and X represent ATP and ADP, respectively. State YLX can transition to state XLY, exporting X to the IMS and importing Y, following unbinding of the molecules. The productive transition that exports ATP is DLT → TLD, and the reversal reaction imports ATP to the matrix and exports ADP to the IMS. Two additional states (DLD′ and TLT′) were added to track futile translocation (exchange of ADP for ADP and ATP for ATP). Starting from previously fitted flux parameters (Metelkin et al., 2006) for ANTs extracted from heart mitochondria (Krämer and Klingenberg, 1982), we first estimated the parameters of the dynamic implementation of the model. With this set of parameters, we qualitatively reproduced the independent data from published work (Krämer and Klingenberg, 1982; Duyckaerts et al., 1980). The list of the reactions is given in Table 3. The rate constants of the model are presented in Tables 4 and 5, and the qualitative reproduction of the experimental data is given in Fig. S1 and Fig. S2. Additional information about the experiments and comparisons with other models can be found in the supplemental text at the end of the PDF.

Thermodynamic constraints

As presented in the previous section, the parameters of the ANT model are constrained by thermodynamic considerations (Eq. 1). If we consider a positive cycle as a productive translocation of one ATP from the matrix to the IMS and ADP from the IMS to the matrix (Fig. 2 G), the product of the rate constants in the positive cycle ($\prod_{k+}$) divided by the product of the rate constants in the negative cycle ($\prod_{k-}$) can be written as:

Table 3. List of reactions for the ANT model

List of reactions for the ANT model
$T_m + L \underset{k_{T_m}^-}{\overset{k_{T_m}^+}{\rightleftharpoons}} LT$
$D_m + L \underset{k_{D_m}^-}{\overset{k_{D_m}^+}{\rightleftharpoons}} LD$
$T_i + L \underset{k_{T_i}^-}{\overset{k_{T_i}^+}{\rightleftharpoons}} TL$
$D_i + L \underset{k_{D_i}^-}{\overset{k_{D_i}^+}{\rightleftharpoons}} DL$
$T_i + LT \underset{k_{T_i}^-}{\overset{k_{T_i}^+}{\rightleftharpoons}} TLT$
$D_i + LT \underset{k_{D_i}^-}{\overset{k_{D_i}^+}{\rightleftharpoons}} DLT$
$T_i + LD \underset{k_{D_i}^-}{\overset{k_{D_i}^+}{\rightleftharpoons}} TLD$
$D_i + LD \underset{k_{D_i}^-}{\overset{k_{D_i}^+}{\rightleftharpoons}} DLD$
$TLD \xrightarrow{k_{cp}} DLT$
$DLT \xrightarrow{k_p} TLD$
$TLT \xrightarrow{k_t} TLT'$
$TLT' \xrightarrow{k_t} TLT$
$DLD \xrightarrow{k_d} DLD'$
$DLD' \xrightarrow{k_d} DLD$

$$\frac{\prod k^+}{\prod k^-} = \frac{k_{T_m}^+ [T_m] k_{D_i}^+ [D_i] k_p k_{T_i}^- k_{D_m}^-}{k_{D_m}^+ [D_m] k_{T_i}^+ [T_i] k_{cp} k_{D_i}^- k_{T_m}^-}. \tag{30}$$

Here, k^- is the backward rate constant and k^+ is the forward rate constant for ATP (T) or ADP (D) from the matrix side (m) or the IMS (i), respectively. Replacing with the dissociation constants (the ratio of the backward to forward reaction rates), we arrive at:

$$\frac{\prod k^+}{\prod k^-} = \frac{K_{T_i} K_{D_m} k_p [T_m][D_i]}{K_{D_i} K_{T_m} k_{cp} [D_m][T_i]}, \tag{31}$$

where $[D_m]$, $[T_m]$, $[T_i]$, and $[D_i]$ are the concentrations of ADP and ATP in the matrix and IMS, respectively. The Gibbs free energy per mole associated with the species before the translocation is:

$$\begin{aligned} G_i &= RT\ln([T_m]) + z_t F\psi_1 + RT\ln([D_i]) + z_D F\psi_4, \\ G_o &= RT\ln([T_i]) + z_t F\psi_4 + RT\ln([D_m]) + z_D F\psi_1, \end{aligned} \tag{32}$$

where z_t and z_d are the charges of the ionized forms of ATP and ADP, –4 and –3, respectively. So, the difference in Gibbs free energy per mole associated with the translocation of an ionized ATP molecule from the matrix to the IMS against a concentration gradient and the translocation of an ionized ADP molecule from the matrix to the IMS is equal to

Table 4. Parameters for the ANT model at Δψ = 180 mV

Parameter	Value	Unit
$k_{T_m}^-$	4×10^4	s^{-1}
$k_{T_m}^+$	6.4×10^6	$M^{-1}s^{-1}$
$k_{T_i}^-$	200	s^{-1}
$k_{T_i}^+$	4×10^5	$M^{-1}s^{-1}$
$k_{D_m}^-$	4×10^4	s^{-1}
$k_{D_m}^+$	4×10^6	$M^{-1}s^{-1}$
$k_{D_i}^-$	100	s^{-1}
$k_{D_i}^+$	4×10^6	$M^{-1}s^{-1}$
k_p	9.2	s^{-1}
k_{cp}	0.35	s^{-1}
k_d	0.48	s^{-1}
k_t	0.58	s^{-1}
T	310	K
$\Delta\psi$	180	mV
δ_{ANTs}	1.37	nmol/mg prot[a]
#ANTs$_1$	16,471[b]	

[a]We estimated 1 nmol/mg ≈ 1.25 mM.
[b]We used the volume of the IM to get the final number of ANTs.

$$\Delta G = G_i - G_o = RT\ln\left(\frac{[T_m][D_i]}{[T_i][D_m]}\right) + F(\psi_4 - \psi_1). \tag{33}$$

Combining Eq. 31 and Eq. 33 we arrive at:

$$\frac{K_{T_i} K_{D_m} k_p [T_m][D_i]}{K_{D_i} K_{T_m} k_{cp} [D_m][T_i]} = e^{\ln\frac{[T_m][D_i]}{[T_i][D_m]}} e^{\frac{F\Delta\psi}{RT}}, \tag{34}$$

Table 5. Parameters for the ANT model at Δψ = 0 mV

Parameter	Value	Unit
$k_{T_m}^-$	4.4×10^4	s^{-1}
$k_{T_m}^+$	6.4×10^6	$M^{-1}s^{-1}$
$k_{T_i}^-$	200	s^{-1}
$k_{T_i}^+$	4.8×10^6	$M^{-1}s^{-1}$
$k_{D_m}^-$	4×10^4	s^{-1}
$k_{D_m}^+$	4×10^6	$M^{-1}s^{-1}$
$k_{D_i}^-$	100	s^{-1}
$k_{D_i}^+$	4×10^6	$M^{-1}s^{-1}$
k_p	0.15	s^{-1}
k_{cp}	0.35	s^{-1}
k_d	0.48	s^{-1}
k_t	0.78	s^{-1}
T	310	K
$\Delta\psi$	0	mV

Garcia et al.
Mitochondrial morphology governs ATP production rate

Journal of General Physiology 7 of 16
https://doi.org/10.1085/jgp.202213263

which reduces to:

$$\frac{K_{T_i}K_{D_m}k_p}{K_{D_i}K_{T_m}k_{cp}} = e^{\frac{F\Delta\psi}{RT}}. \tag{35}$$

This equation summarizes the imposing restrictions on the rate constants.

The differential equations for the number of molecules of the ANT model in the different states are:

$$\frac{dL}{dt} = -(k_{T_i}^+T_i+k_{T_m}^+T_m+k_{D_i}^+D_i+k_{D_m}^+D_m)L + k_{T_i}^-TL + k_{T_m}^-LT + k_{D_i}^-DL$$
$$+k_{D_m}^-LD,$$

$$\frac{dTL}{dt} = k_{T_i}^+T_iL - (k_{T_i}^-+k_{D_m}^+D_m+2k_{T_m}^+T_m)TL + k_{T_m}^-TLT + k_{T_m}^-TLT'$$
$$+k_{D_m}^-TLD,$$

$$\frac{dLT}{dt} = k_{T_m}^+T_mL - (k_{T_m}^-+k_{D_i}^+D_i+2k_{T_i}^+T_i)LT + k_{T_i}^-TLT + k_{T_i}^-TLT'$$
$$+k_{D_i}^-DLT,$$

$$\frac{dDL}{dt} = k_{D_i}^+D_iL - (k_{D_i}^-+k_{T_m}^+T_m+k_{D_m}^+D_m)DL + k_{D_m}^-DLD + k_{D_m}^-DLD'$$
$$+k_{T_m}^-DLT,$$

$$\frac{dLD}{dt} = k_{D_m}^+D_mL - (k_{D_m}^-+k_{T_i}^+T_i+k_{D_i}^+D_i)LD + k_{D_i}^-DLD + k_{D_i}^-DLD'$$
$$+k_{T_i}^-TLD,$$

$$\frac{dTLD}{dt} = k_{D_m}^+D_mTL + k_{T_i}^+T_iLD - (k_{D_m}^-+k_{cp})TLD + k_pDLT - k_{T_i}^-TLD,$$

$$\frac{dDLD}{dt} = k_{D_i}^+0.5D_iLD + k_{D_m}^+0.5D_mDL - (k_{D_i}^-+k_{D_m}^-+k_d)DLD + k_dDLD',$$

$$\frac{dDLD'}{dt} = k_{D_i}^+0.5D_iLD + k_{D_m}^+0.5D_mDL - (k_{D_i}^-+k_{D_m}^-+k_d)DLD' +k_dDLD,$$

$$\frac{dTLT}{dt} = k_{T_i}^+0.5T_iLT + k_{T_m}^+0.5T_mTL - (k_{T_i}^-+k_{T_m}^-+k_t)TLT + k_tTLT',$$

$$\frac{dTLT'}{dt} = k_{T_i}^+0.5T_iLT + k_{T_m}^+0.5T_mTL - (k_{T_i}^-+k_{T_m}^-+k_t)TLT' +k_tTLT. \tag{36}$$

A vast majority of the models do not consider ATP and ADP concentrations as variables (Magnus and Keizer, 1997; Cortassa et al., 2003). Because we focused on the local cytosolic environment around a single mitochondrion, we consider ATP and ADP concentrations in the different compartments as variables. To account for their dynamics, we also derived the equations for the number of ATP and ADP molecules in the different compartments:

$$\frac{dD_m}{dt} = -(k_{D_m}^+L + k_{D_m}^+TL + k_{D_m}^+DL + k_{43}H_3E_o)D_m+k_{D_m}^-LD + k_{D_m}^-TLD,$$
$$+k_{D_m}^-DLD + k_{D_m}^-DLD' +k_{34}H_3ES, \tag{37}$$

$$\frac{dT_m}{dt} = -(k_{T_m}^+L + k_{T_m}^+TL + k_{T_m}^+DL + k_{23}H_3E)T_m+k_{T_m}^-LT + k_{T_m}^-DLT,$$
$$+k_{T_m}^-TLT + k_{T_m}^-TLT' +k_{32}H_3ES, \tag{38}$$

$$\frac{dT_i}{dt} = -(k_{T_i}^+L + k_{T_i}^+LT + k_{T_i}^+LD + k_pn_{vdac})T_i+k_{T_i}^-TL + k_{T_i}^-TLD,$$
$$+k_{T_i}^-TLT + k_{T_i}^-TLT' +k_pT_{cyto}n_{vdac}, \tag{39}$$

$$\frac{dT_{cyto}}{dt} = n_{vdac}k_{vdac}T_i - n_{vdac}k_{vdac}T_{cyto}, \tag{40}$$

where D_m is the number of ADP molecules in the matrix, T_m is the number of ATP molecules in the matrix, D_i is the number of ADP molecules in the IMS, T_i is the number of ATP molecules in the IMS, and T_{cyto} is the number of ATP molecules in the cytosol. These numbers were set by converting the concentration in each compartment to the number of molecules for each reconstruction (see Metabolite buffers), and these were the initial conditions considered. The number of VDACs on the OM is represented as n_{vdac} in these equations (this parameter is #VDACs$_1$ in Table 6 for reconstruction #1).

As before, the rate constants of the bimolecular reactions have been normalized to have proper units to compute the number of particles, i.e., $k = \frac{k'}{N_A*V}$, where k' represents the constants given in Table 4, N_A is Avogadro's number, and V represents the volume.

As for the ATP synthase model, the total number of ANTs is a conserved quantity ($L_{tot} = L + DL + DLD + DLD' + TL + LT + TLT + TLT' + DLT + TLD$). L_{tot} is the total number of ANTs considered in our simulations; for the mitochondrial reconstruction #1, this quantity is 16,471 (this parameter is #ANTs$_1$ in Table 4).

Molecular VDAC model

The main mechanism for metabolites to cross the OM is through VDACs. To consider the ATP export from the IMS into the cytosol, we included VDACs. We implemented a rather simple model assuming VDAC proteins interact with ATP molecules and translocate them to the cytosol by the reaction $VDAC + ATP_{IMS} \rightleftharpoons VDAC + ATP_{cyto}$. The list of parameter values employed is given in Table 6.

Metabolite buffers

The total concentration of ATP and ADP can be distributed in different compounds or states like ATP^{4-}, ADP^{3-}, ATPMg^{2-}, etc. ATP and ADP can react with different cations, or be bound or ionized. The final distributions can be estimated by coefficients representing the fraction of unbound ATP in the matrix or the other compartments, and these proportions are determined mainly by the level of Mg^{2+}. For our model, mitochondrial ADP^{3-} and ATP^{4-} concentrations were estimated analogously to a previous work (Magnus and Keizer, 1997). These estimations are based on experimental data (Corkey et al., 1986).

Table 7. Volumes and surface areas of the different compartments considered in the model

Property	Mito 1	Mito 2	Mito 4	Mito 5	Mito 8	Mito 9	Mito 10	Mito 11	Mito 12
OM vol (μm^3)	0.037	0.029	0.012	0.012	0.014	0.006	0.016	0.009	0.021
IM vol (μm^3)	0.016	0.010	0.005	0.004	0.006	0.002	0.008	0.003	0.010
IM SA (μm^2)	1.545	1.104	0.505	0.390	0.508	0.224	0.605	0.314	0.806
High curva IM SA (μm^2)	0.087	0.049	0.037	0.015	0.042	0.032	0.067	0.023	0.115
Cyto vol (μm^3)	0.306	0.061	0.094	0.048	0.101	0.050	0.108	0.111	0.148
#ATP$_{syn}$	267	150	114	46	129	98	204	72	353
#ANTs	16,471	10,294	5,398	4,118	6,177	2,570	7,905	3,578	10,294
#VDACs	6,340	5,990	2,816	3,370	3,560	1,788	3,126	2,558	3,970

These measurements were taken from nine realistic 3-D reconstructions of presynaptic and axonal mitochondria (Mendelsohn et al., 2021). The volume of the cytosol (Cyto vol) is an arbitrary volume. The numbers of proteins considered for each simulation were determined using the densities (Tables 2, 4, and 6) and respective surface areas or volumes. To determine the number of ATP synthases, the areas of high curvature (Mendelsohn et al., 2021) were considered (high curva IM SA), and values of the first principal curvature larger than 70 μm^{-1} were assessed.

The approximate distributions are $[ADP]_{m,free} = 0.8\ [ADP]_m$, $[ATP]_{m,free} = [ATP]_m$, $[ATP^{4-}] = 0.05\ [ATP]_{free}$, and $[ADP^{-3}] = 0.45\ [ADP]_{free}$.

The initial concentrations of ATP and ADP in the IMS and cytosol were set to 6.5 and 0.1 mM, respectively (Mörikofer-Zwez and Walter, 1989; Cunningham et al., 1986). The initial concentrations of ATP and ADP in the matrix were set to 13 and 2 mM (15 mM in total), respectively. The total concentration of adenylates in the matrix (ATP + ADP) of liver mitochondria is in the range of 2–27 mM (Rulfs and Aprille, 1982; Nosek et al., 1990; Austin and Aprille, 1984), in the same range for heart mitochondria (Livingston et al., 1996), and also ~15 mM for pancreatic cells (Magnus and Keizer, 1997). Moreover, the ratio of ATP to ADP in the matrix has been estimated to be about 10 (Nicholls, 2013). These results are consistent with our assumption of an initial concentration of 13 mM of ATP and 2 mM of ADP in the matrix. In some simulations, these concentrations were kept constant. The concentrations were converted to the number of molecules using the volumes of the different compartments (see Table 7).

Simulation methods
System of ODEs
The system of ODEs has a total of 19 equations and 41 parameters, including chemical rate constants, volumes, and number of proteins. The volumes of the different compartments are listed in Table 7. We used reconstruction #1 for all the non-spatial simulations.

Eqs. 29, 37, and 40 were integrated using a Radau stiff integrator in PyDSTool (version 1.19.2; Clewley et al., 2007).

Spatial simulations
To perform spatiotemporal simulations in realistic 3-D reconstructions, we implemented the set of reactions in MCell version 4.0 (Kerr et al., 2008; Stiles et al., 1996; Husar et al., 2022 *Preprint*), an agent-based reaction–diffusion simulator. The model is built using the set of reactions described in Tables 1 and 3. Previous research showed that ATP synthases accumulate at

the rim of the cristae membrane in lamellar cristae and along the length of tubular cristae (Strauss et al., 2008; Davies et al., 2012). To emulate this organization in our reconstructions, we selected the areas of high curvature in the cristae membrane (Mendelsohn et al., 2021) and we randomly distributed them in these areas. The areas of high curvature were identified as vertices of the cristae membrane with the first principal curvature higher than 70 μm^{-1}. The location of ANTs in mitochondria has not been definitively resolved, and experimental evidence shows they may form complexes with ATP synthases (Ko et al., 2003) located in the cristae membrane (CM; Wittig and Schägger, 2009; Vogel et al., 2006). Therefore, we randomly distributed ANTs in the areas of high curvature as well. VDACs were homogeneously distributed on the OM. ATP and ADP molecules were homogeneously distributed in the respective compartments. The diffusion coefficient considered for the free forms of ATP and ADP is 1.5×10^{-7} cm^2 s^{-1}.

Online supplemental material
In Figs. S1 and S2, we compared experimental results from Krämer and Klingenberg (1982) and Duyckaerts et al. (1980) to the results obtained with the ANT translocator model. In Fig. S3, we show ATP fluxes through ANTs generated with the model developed by Bohnensack (1982). In Fig. S4, we present spatial simulation performed with the same conditions considered in the main text, but kept the number of ATP synthases constant in all reconstructions. In Fig. S5, we compare the result with the previously developed version of the mitochondrial model (Garcia et al., 2019) with the current version. Supplemental text appears at the end of the PDF and provides additional information about the experiments and comparisons to other models.

Results
Before studying the dynamics of the assembled model, we first analyzed the behavior of its components separately and compared them with previously developed models. In these first
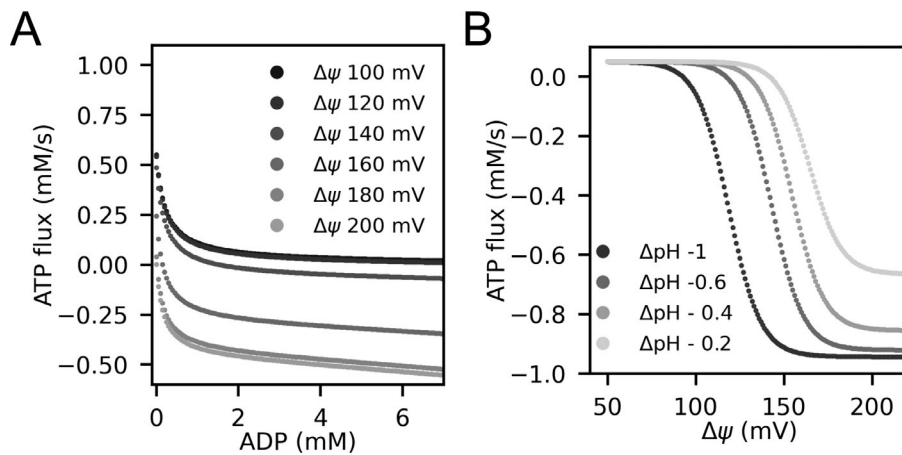
Figure 3. **ATP synthase steady-state flux analysis.** We analyzed the dependence on the fluxes through ATP synthases at constant concentrations of adenine nucleotides in the different compartments. We analyzed how the flux changes with the driving forces of the cycles (Eq. 26). **(A)** ATP net flux through ATP synthases for different concentrations of ADP in the matrix and different membrane potentials. A counterclockwise cycle is defined as positive, favoring ATP hydrolysis. For membrane potentials above 160 mV and larger ADP$_m$ concentrations, ATP is synthesized. **(B)** ATP net flux through ATP synthases for different pH and membrane potentials (for fixed concentrations of adenine nucleotides).

simulations, we assumed steady-state conditions and kept the ADP and ATP concentrations constant in the different compartments. We then conducted dynamic simulations with the ODE representation to understand which is the limiting step in ATP production. Finally, we performed spatial simulations with nine realistic 3-D geometries and related the ATP production rate to the morphology of the organelles.

Steady-state flux analysis for the model components and comparison to previously developed models

First, we analyzed the dependence of the ATP flux on the ADP concentration, membrane potential, and pH for the ATP synthase model. The driving forces of cycle c (Fig. 2 C) are the membrane potential, the pH, and the ratio of the ADP and Pi concentration to the ATP concentration relative to the equilibrium constant (Eq. 26). For these simulations, the ΔpH was set to –0.4 (Tischler et al., 1977) and the total concentration of adenine nucleotides in the matrix was set to 15 mM (Austin and Aprille, 1984; Rulfs and Aprille, 1982). In Fig. 3 A, we show the ATP net flux through ATP synthases for different concentrations of ADP in the matrix. A positive flux is defined in the counterclockwise direction, favoring ATP hydrolysis. We found that at small concentrations of ADP, the flux is positive, meaning ATP is hydrolyzed. Increasing the concentration of ADP in the matrix, the ATP flux becomes negative, indicating that ATP synthesis is favored. The flux saturates at concentrations of ADP above 1 mM. Moreover, the driving forces of the cycle also depend on the membrane potential (Eq. 26). For a membrane potential above 160 mV, the ATP flux is negative for large concentrations of ADP, but for membrane potential below those values, ATP is hydrolyzed. Similar results were obtained for the ATP flux derived by Magnus and Keizer (1997) and later modified by Cortassa et al. (2003) (for comparison see Fig. S6 A in the supplementary material in Cortassa et al. [2003]; the difference in the sign of the fluxes is due to different sign conventions).

Next, we studied the dependence of the ATP flux on the pH difference between the matrix and the IMS (Fig. 3 B). Here, we fixed the pH in the matrix at 7.6 and varied the pH

in the IMS. When the pH difference between the matrix and IMS is large, a smaller membrane potential is needed to observe a negative ATP flux, i.e., to synthesize ATP. This is because the proton motive force—the membrane potential minus the difference in pH (Eq. 21)—drives the protons to the matrix.

The ATP flux also saturates at higher membrane potentials, and in particular is almost saturated at 180 mV—the potential considered for the rest of this work. Similar flux dependencies were observed in the past (for comparison see Fig. S6 B in the supplementary material in Cortassa et al. [2003]), although their maximal flux is about 10 mM s^{-1} while ours is about 0.9 mM s^{-1}. A similar dependence on the membrane potential was also observed by Nguyen et al. (2007) (Fig. 2 D in their paper), and their maximum flux is 1.125 mM s^{-1}, very close to the range in our work.

The driving force of the ANT translocation is the membrane potential and the ratio of ATP$_m$/ADP$_m$ in the matrix and ATP$_i$/ADP$_i$ in the IMS (Eq. 33). Therefore, we studied the dependence of the net ADP$_i$ – ATP$_m$ flux through ANTs at steady concentrations of ATP and ADP for different ratios. First, we calculated the net ADP$_i$ – ATP$_m$ flux through ANTs for different ratios ATP$_m$/ADP$_m$ in the matrix (Fig. 4 A). Keeping the cytosolic ratio fixed at 65, we varied the ATP$_m$/ADP$_m$ ratio. The driving force of the cycle (Eq. 33) increases for larger ATP$_m$/ADP$_m$ ratios, increasing the net ADP$_i$ – ATP$_m$ flux (Fig. 4 A). The net ADP$_i$ – ATP$_m$ flux saturates for ratios ATP$_m$/ADP$_m$ closer to the ratio of ATP$_i$/ADP$_i$ (Eq. 33).

Next, we varied the ATP$_i$/ADP$_i$ ratio in the IMS and kept the matrix ratio constant at 6.5. Increasing the ATP$_i$/ADP$_i$ ratio decreases the driving force (Eq. 33) at a constant ATP$_m$/ADP$_m$ ratio. Therefore, the net ADP$_i$ – ATP$_m$ flux decreases for larger ratios of ATP$_i$/ADP$_i$ (Fig. 4 B). Moreover, the maximum flux is set by the ATP$_m$/ADP$_m$ ratio. Similar flux dependencies were found by Magnus and Keizer (1997) with the model developed by Bohnensack (1982), see Fig. S3.

From this analysis, we identified that for 1 mM ADP$_m$, 180 mV membrane potential, and –0.4 ΔpH, the ATP flux is almost at its maximum absolute value (Fig. 3, A and B). We used these values for the rest of this work. Likewise, the initial concentration
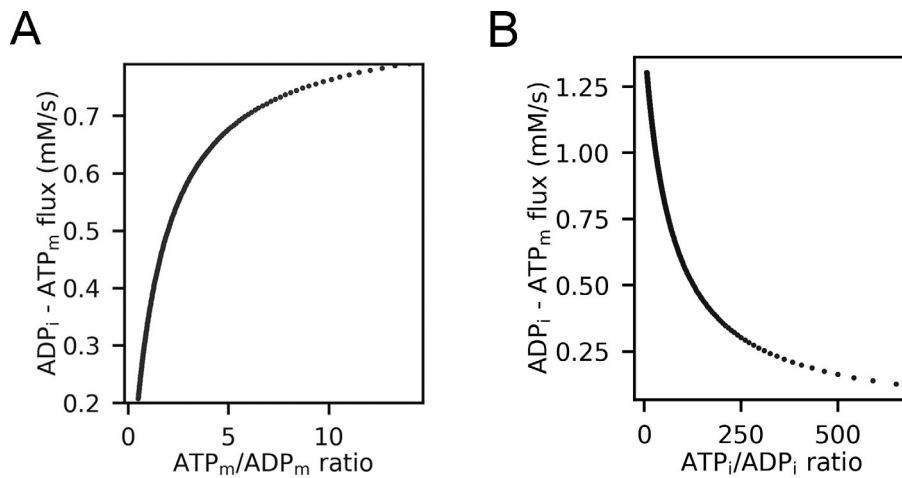
Figure 4. **ANT steady-state flux analysis.** We analyzed the dependence on the fluxes through ANTs at constant concentrations of adenine nucleotides in the different compartments and at a constant membrane potential of 180 mV. We analyzed how the flux changes with the driving forces of the cycles (Eq. 33). **(A)** ADP_i – ATP_m net flux through ANTs for different ATP to ADP ratios in the matrix. **(B)** ADP_i – ATP_m net flux through ANTs for different ratios of ATP and ADP in the IMS.

ratios considered in the rest of this work are ATP_m/ADP_m = 6.5 and ATP_i/ADP_i = 65, from which the ADP_i – ATP_m flux through ANTs is almost at its maximal value.

Under physiological conditions, ATP production is the limiting step for cytosolic ATP availability

The amount of ATP in the cytosol depends on the production rate and its export through ANTs and VDACs. Since experimental results suggest that the ANT translocation rate constants are in the order of 100s per second (Gropp et al., 1999), we explored the impact of fast export through ANTs on the final ATP

concentration in the cytosol. We held the concentration of ADP in the IMS constant and changed the parameters of the ANT model. Specifically, we changed the value of the rate constants k_p, k_{cp}, k_t, and k_d multiplying them by a factor of r, such that detailed balance is still satisfied. We measured the number of ADP and ATP molecules in the matrix (Fig. 5, A and B) and the number of molecules of ATP in the IMS and cytosol (Fig. 5, C and D). Faster translocation allows more ADP to accumulate in the matrix (Fig. 5 A) and therefore less ATP (Fig. 5 B), while ATP molecules reach the IMS and the cytosol faster (Fig. 5, C and D). We further calculated the percentage of the ATP increase
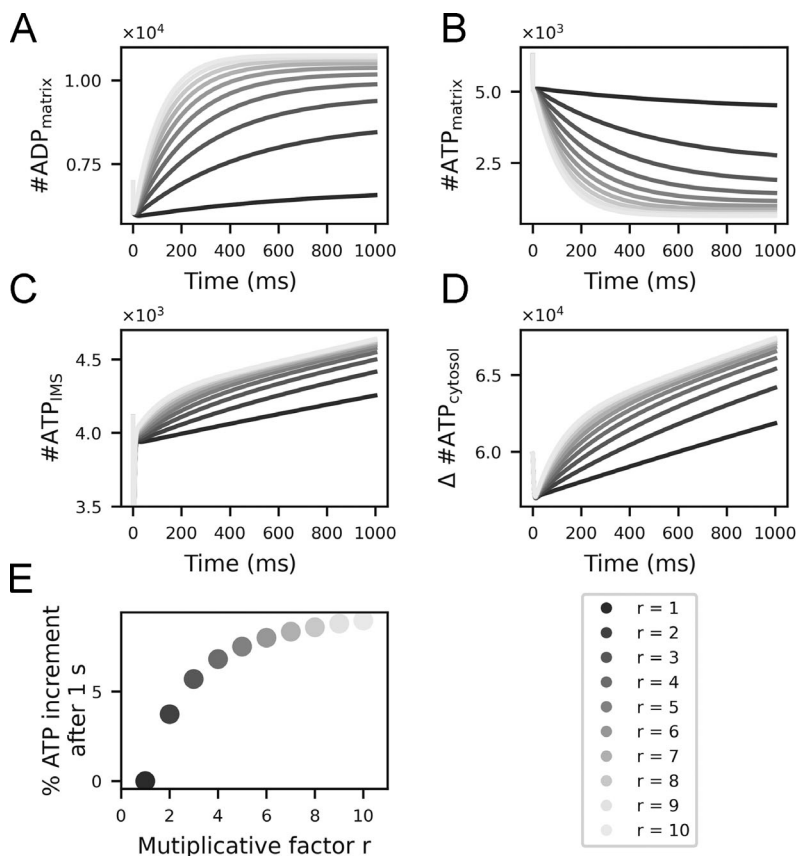

Figure 5. **Parameter exploration for the ANT model at a constant membrane potential of 180 mV.** We employed the ODE model to explore the impact of faster ANTs on ATP production, and for that, we changed the rate constants of the ANTs. We multiplied the rate constants k_p, k_{cp}, k_t, and k_d by a factor of r, where r takes values between 1 and 10. The ADP concentration in the IMS was kept constant in these simulations. **(A–C)** Number of molecules measured over time in the different compartments. **(D)** Number of ATP molecules measured over time in the cytosol relative to the initial number of molecules. **(E)** Percentage increment of the number of ATP molecules in the cytosol after 1 s relative to the slowest ones (r = 1), for all ANTs considered from the slowest (r = 1) ones to the fastest ones (r = 10).
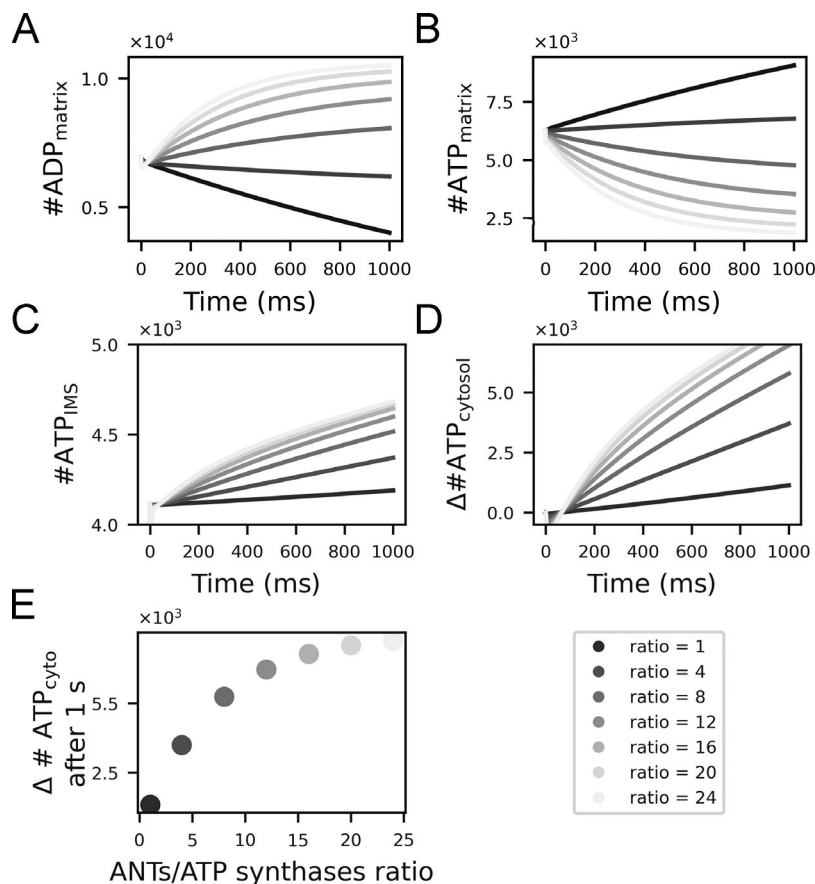
Figure 6. **What is the limiting factor, export through ANTs or production of ATP through ATP synthases?** We changed the ratio of ANTs to ATP synthases to answer this question and used the ODE model to estimate the impact on ATP production, for a constant concentration of ADP in the IMS and a constant membrane potential of 180 mV. **(A–C)** Number of molecules measured over time in the different compartments. **(D)** Number of ATP molecules measured over time in the cytosol relative to the initial number. **(E)** Number of ATP molecules in the cytosol after 1 s relative to the initial number of molecules, for different ratios of ANTs/ATP synthases. Ratios go from 1 to 24, the number of ATP synthases is kept constant, and the number of ANTs increases (fast ANTs were considered r = 10).

relative to the slowest import (Fig. 5 E). The fastest ANTs (r = 10) exports 10% more ATP molecules than the slowest ones. Moreover, the amount of ATP starts to saturate for the fastest ANTs (r = 10). This means even ANTs that are faster cannot overcome the ATP production rate. Thus, the rate-limiting step is the ATP production rate, not the export.

In addition to the translocation rate of the ANTs, the ratio of ANTs to the ATP synthases can influence the export of ATP molecules into the cytosol. Therefore, we next asked how this ratio affects the availability of ATP in the cytosol for the fastest ANTs. We asked which step limits the number of ATP molecules in the cytosol under these conditions—is it the synthesis of ATP or its translocation through ANTs? As in the previous simulations, the number of ADP molecules in the IMS was constant, assuming unlimited resources. We measured the number of ADP and ATP molecules in the matrix, IMS, and cytosol over time (Fig. 6, A–D).

The amount of ATP in the cytosol after 1 s starts to saturate when the number of ANTs is 20 times the number of ATP synthases (Fig. 6 E). Thus, our model predicts that having more than 20 times ANTs to the number of ATP synthases will not have any benefit. If this ratio is bigger than 20, the limiting step is the production of ATP.

Similarly, VDACs can limit the amount of ATP in the cytosol. Therefore, we analyzed how the export of ATP through VDACs limits their amount in the cytosol. Considering similar conditions as before the constant concentration of ADP in the IMS,

we changed the number of VDACs in the OM and measured the number of ADP and ATP in the different compartments (Fig. 7, A–D), along with the percentage increment of ATP in the cytosol after 1 s (Fig. 7 F). Having less than ~500 VDACs in the OM significantly limits the amount of ATP available in the cytosol. Otherwise, the production of ATP is the limiting step.

Given the density of VDACs in the OM (De Pinto et al., 1987) and the surface area of the OM measured (Mendelsohn et al., 2021; see Materials and methods), the number of VDACs in reconstruction #1 is 6,340. This number is well above the limiting threshold of 500. Therefore, in the physiological conditions we considered, the production of ATP is the limiting step.

Spatial simulations: Application of the model to different 3-D mitochondrial reconstructions

To illustrate the utility of our model, we conducted spatial simulations with nine realistic 3-D reconstructions (Mendelsohn et al., 2021) using the agent-based reaction–diffusion simulator MCell, and we related the ATP production rate to morphological features of mitochondria. In Fig. 8 A, we show the CM of the nine reconstructions with the total number of ATP synthases considered for the simulations (in red). In Fig. 8 B, we show the results of the ODE system and averaged traces of the spatial simulations (over 10 different realizations) of the number of ADP and ATP in the different compartments for the elongated mitochondrial reconstruction #2 for the same conditions considered as before.
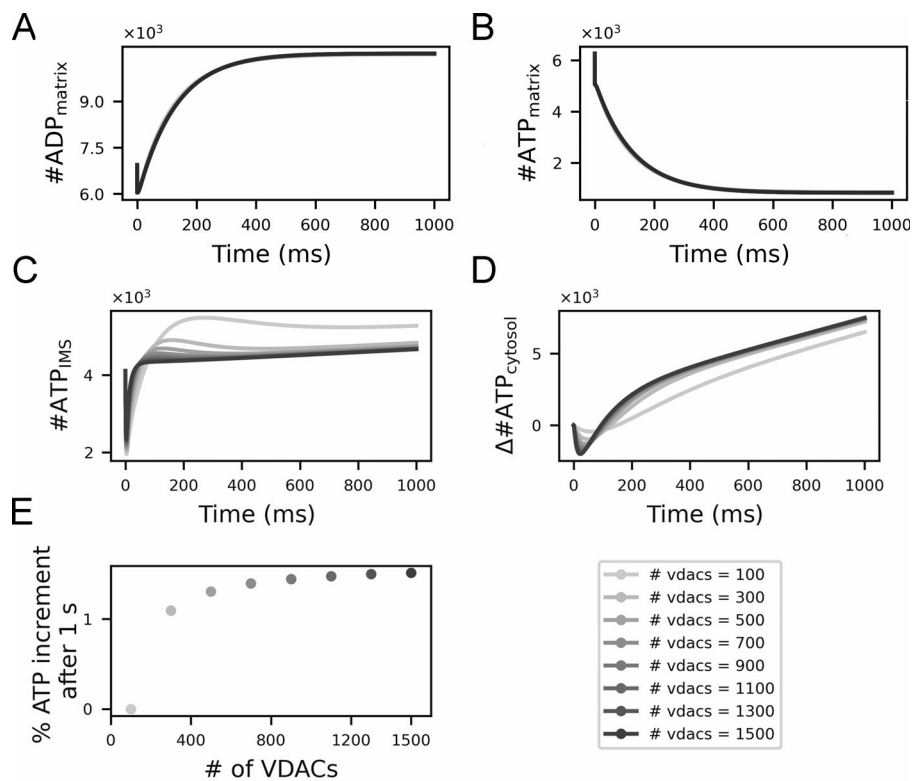
Figure 7. **Effect of the number of VDACs on ATP efflux to the cytosol at a constant membrane potential of 180 mV. (A–C)** Number of molecules measured over time in different compartments. **(D)** Number of ATP molecules measured over time in the cytosol relative to the initial concentration. **(E)** Percentage increase of ATP in the cytosol after 1 s for different numbers of VDACs in the OM. The number of VDACs goes from 100 to 1,500 (in these simulations fast ANTs were considered, r = 10).

Using tools from differential geometry, we recently analyzed the structural features of these reconstructions, and based on this analysis we group them into two categories: globular organelles and elongated ones (Mendelsohn et al., 2021; Fig. 8 A). Organelles in the globular group have larger surface area formed by vertices with high curvature. Large curved-surface areas correspond to more number of ATP synthases in these reconstructions.

We performed spatial simulations for all reconstructions and measured the ATP production rate in the cytosol for each reconstruction. For that, we performed a linear regression to single traces of the number of ATP molecules in the cytosol over time. Averaged rates are shown in Fig. 8 C. As expected from our analysis, the ATP production rate in the cytosol is larger for globular organelles, which have larger areas of high curvature. For comparison, we also performed simulation with the same number of ATP synthases in all reconstructions. The results can be found in Fig. S4.

Discussion

Given the indispensable nature of mitochondria in cellular energy production, having accurate models of mitochondrial dynamics is critical for understanding their impact on cellular function.

In this work, we focused on developing a thermodynamically consistent model of ATP production in mitochondria to ensure the model is physically plausible. In doing so, we derived the relationships for the dependence of kinetic parameters on the membrane potential, proton, and substrate concentration.

We explored different parameter regimes to understand in which conditions ATP production or its export are the limiting

steps in making ATP available in the cytosol. Under the conditions considered, we found two regimes: at a low ratio of ANTs to ATP synthases, the export of ATP is limited by the ANTs. At ratios higher than 20:1, the ATP production becomes the limiting step. Similarly, the number of VDACs does not limit the export of ATP, unless there are very few VDACs present (in the order of 100s, for the ratio of ANTs/ATP synthases considered).

Finally, we performed spatial simulations on nine mitochondrial reconstructions derived from electron microscopy data. According to our parameter exploration, the number of ANTs and VDACs in these nine reconstructions are such that the synthesis of ATP is the limiting step on the ATP production rate in the cytosol and not its export. We further measured the rate for the same conditions and relate this quantity to the structural features of the organelles. We had mapped features of the OM to features of the IM recently in Mendelsohn et al. (2021) with tools from differential geometry, and showed that globular organelles—characterized by smaller aspect ratio and smaller average first principal curvature of the OM—have larger curved CM surface areas. These organelles also have other features of high energy capacity like a large crista shape factor and a high number of crista junctions per OM surface area. Others have shown that mitochondria at high-energy-demanding locations in outer hair cells of young mice (Perkins et al., 2020), as well as mitochondria from high-spiking interneurons (Cserép et al., 2018), show a large crista shape factor and a high number of crista junctions per OM surface area. These features are also characteristic of our globular set, which suggests a high level of metabolic activity for such mitochondria. Here, using our mathematical model, we found that globular organelles generate more ATP in the cytosol than the elongated morphologies (Fig. 8 C).
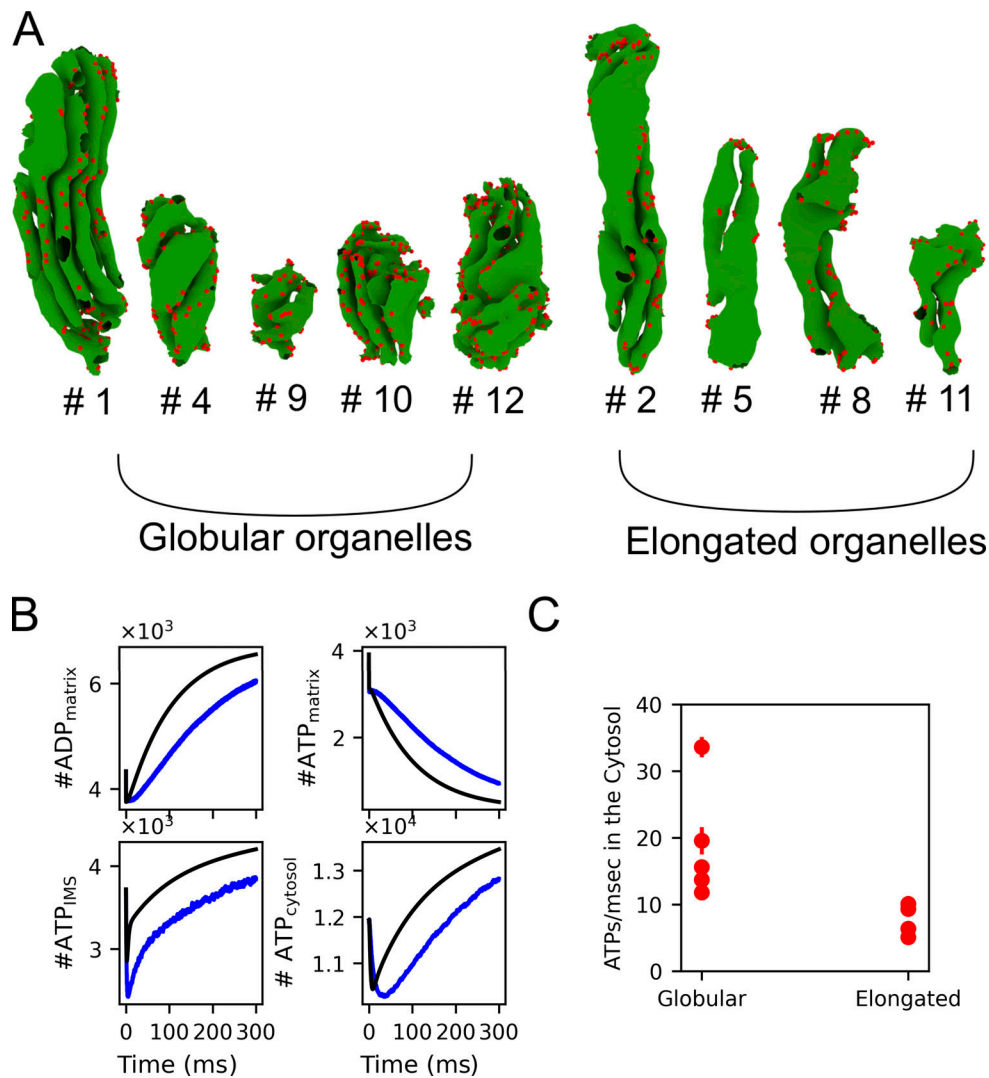
Figure 8. **Spatial simulations: linking structure to function. (A)** CM of the nine mitochondrial reconstructions considered with ATP synthases (in red) distributed in the areas of high curvature. **(B)** Comparison of the ODEs simulations with the average traces of the spatial simulations for elongated mitochondrial reconstruction #2. **(C)** ATP production rate in the cytosol for all reconstructions grouped accordingly to the structural features.

The maximum rate measured with our spatial model is roughly 30 ATPs/ms (Fig. 8 C), and this corresponds to 170 μM s⁻¹ (considering the volume of the cytosol). Recent measurements in myocytes (Wescott et al., 2019) estimated the ATP production rate in the range of 200–600 μM s⁻¹ depending on the calcium concentration. The organelles considered in this manuscript are axonal and presynaptic reconstructions and are small (in the range of 0.037 to 0.012 μm³) compared with organelles in myocytes (in the order of 0.5 μm³; Laguens, 1971). This could explain our smaller ATP production rate in the cytosol.

We acknowledge that our modeling approach has a number of limitations. First, the membrane potential in our simulations is constant, and we emulate a constant state of ATP production. Second, the ATP synthase flux considered in our model saturates sigmoidally at large membrane potentials (Fig. 3 B), as it has been shown for *Propionigenium modestum* bacteria and *Escherichia coli* (Kaim and Dimroth, 1999), and is more sensitive to

changes in the membrane potential than to ΔpH. However, recent experiments on heart and skeletal mitochondria (Wescott et al., 2019) show no saturation of the ATP synthase flux when increasing the membrane potential. Our model does not reproduce this behavior. Its voltage dependence is a consequence of the detailed dynamic of the ATP synthase model (Pietrobon and Caplan, 1985), which is drawn from physical assumptions about the rate constants, the membrane potential, and the pH concentration. Taking different assumptions or expanding the number of states could perhaps give a different flux membrane potential dependence. Third, the Mg²⁺-bound forms of ADP and ATP are the main substrates of ATP synthase in mitochondria. Since our goal was to generate a spatial model of a mitochondrion and Mg²⁺ is found in large concentrations in the matrix, we considered the free form of ADP as the main substrate for ATP production. This is an approximation due to the limitations of using an agent-based model. However, this approximation has been taken in many mitochondrial models in the past

(Magnus and Keizer, 1997; Bertram et al., 2006; Cortassa et al., 2003), and is accepted in the community (Gnaiger, 2020).

Different approaches can be taken to model the spatial organization of mitochondria: from continuum approximations (Leung et al., 2021; Afzal et al., 2021) to discrete descriptions as we considered in our spatial simulations (with an agent-based reaction-diffusion simulator). Well-mixed continuum approximations based on concentrations like those in Leung et al. (2021) and Afzal et al. (2021) break down at low particle numbers. A discrete particle-based approach, as we considered in our spatial simulations with an agent-based reaction-diffusion simulator, is more accurate in this scenario (Bartol et al., 2015). Continuum approaches could be more challenging to integrate into complex geometries. Since we want to explore the impact of the complex mitochondrial morphology on ATP production and include the specialized location of ATP synthases at the rim of the cristae, we opted for a discrete description in our spatial simulations.

These different approaches can lead to similar results. For instance, in the past, we observed gradients of ATP with our discrete approach (Garcia et al., 2019), and so did Afzal et al. (2021), with a continuum description. Our earlier version of the model (Garcia et al., 2019) is based on the same published data (Pietrobon and Caplan, 1985; Metelkin et al., 2006; Magnus and Keizer, 1997). The major improvement of the current version is that the parameters were constrained by thermodynamic considerations (Hill, 1989). The results, however, are consistent (in Fig. S5 we compare for reconstruction #1 both versions of the model).

Finally, our results have implications for our understanding of disease states. For instance, near-total loss of ATP synthase dimerization caused by a neurodegenerative mutation generated profound disturbances of mitochondrial crista ultrastructure in neurons derived from a Leigh syndrome patient (Siegmund et al., 2018). The main architectural feature different from control cells is an increment in the angle of curvature at the tips of the cristae. This feature relates to our curvature measurement of the CM, which directly relates to the total number of ATP synthases. Altered mitochondrial structures have also been shown in aged animals (Perkins et al., 2020; Glavis-Bloom et al., 2023). Further investigation using the methods developed here will allow a deeper understanding of potentially impaired mitochondrial mechanisms in disease states.

Data availability
All the material associated with this work is available in the repository: https://github.com/RangamaniLabUCSD/spatial_mito_model.

References
Acehan, D., A. Malhotra, Y. Xu, M. Ren, D.L. Stokes, and M. Schlame. 2011. Cardiolipin affects the supramolecular organization of ATP synthase in mitochondria. *Biophys. J.* 100:2184–2192. https://doi.org/10.1016/j.bpj.2011.03.031

Afzal, N., W.J. Lederer, M.S. Jafri, and C.A. Mannella. 2021. Effect of crista morphology on mitochondrial ATP output: A computational study. *Curr. Res. Physiol.* 4:163–176. https://doi.org/10.1016/j.crphys.2021.03.005

Alberts, B., K. Roberts, J. Lewis, D. Bray, K. Hopkin, A.D. Johnson, P. Walter, and M. Raff. 2015. Essential Cell Biology. Fourth edition. Garland Science, New York City.

Austin, J., and J.R. Aprille. 1984. Carboxyatractyloside-insensitive influx and efflux of adenine nucleotides in rat liver mitochondria. *J. Biol. Chem.* 259:154–160. https://doi.org/10.1016/S0021-9258(17)43634-9

Balbir, T. 2007. A model of mitochondrial calcium induced calcium release. PhD thesis. Doctoral dissertation The Ohio State University, Columbus, OH. 134 pp.

Bartol, T.M., D.X. Keller, J.P. Kinney, C.L. Bajaj, K.M. Harris, T.J. Sejnowski, and M.B. Kennedy. 2015. Computational reconstitution of spine calcium transients from individual proteins. *Front. Synaptic Neurosci.* 7:17. https://doi.org/10.3389/fnsyn.2015.00017

Beard, D.A. 2005. A biophysical model of the mitochondrial respiratory system and oxidative phosphorylation. *PLoS Comput. Biol.* 1:e36. https://doi.org/10.1371/journal.pcbi.0010036

Bertram, R., M. Gram Pedersen, D.S. Luciani, and A. Sherman. 2006. A simplified model for mitochondrial ATP production. *J. Theor. Biol.* 243: 575–586. https://doi.org/10.1016/j.jtbi.2006.07.019

Bohnensack, R. 1982. The role of the adenine nucleotide translocator in oxidative phosphorylation. A theoretical investigation on the basis of a comprehensive rate law of the translocator. *J. Bioenerg. Biomembr.* 14: 45–61. https://doi.org/10.1007/BF00744078

Caplan, S.R. 1981. Reciprocity or near-reciprocity of highly coupled enzymatic processes at the multidimensional inflection point. *Proc. Natl. Acad. Sci. USA.* 78:4314–4318. https://doi.org/10.1073/pnas.78.7.4314

Caplan, S.R., and A. Essig. 1983. Bioenergetics and Linear Nonequilibrium Thermodynamics. Vol. 3. Harvard University Press, Cambridge, MA. https://doi.org/10.4159/harvard.9780674732063

Clewley, R.H., W.E. Sherwood, M.D. LaMar, and J.M. Guckenheimer. 2007. PyDSTool, a software environment for dynamical systems modeling. http://pydstool.sourceforge.net. (accessed October 10, 2020)

Colombini, M. 2004. VDAC: The channel at the interface between mitochondria and the cytosol. *Mol. Cell. Biochem.* 256-257:107–115. https://doi.org/10.1023/B:MCBI.0000009862.17396.8d

Corkey, B.E., J. Duszynski, T.L. Rich, B. Matschinsky, and J.R. Williamson. 1986. Regulation of free and bound magnesium in rat hepatocytes and isolated mitochondria. *J. Biol. Chem.* 261:2567–2574. https://doi.org/10.1016/S0021-9258(17)35825-8

Cortassa, S., M.A. Aon, E. Marbán, R.L. Winslow, and B. O'Rourke. 2003. An integrated model of cardiac mitochondrial energy metabolism and calcium dynamics. *Biophys. J.* 84:2734–2755. https://doi.org/10.1016/S0006-3495(03)75079-6

Cserép, C., B. Pósfai, A.D. Schwarcz, and Á. Dénes. 2018. Mitochondrial ultrastructure is coupled to synaptic performance at axonal release sites. *eNeuro.* 5:ENEURO.0390-17.2018. https://doi.org/10.1523/ENEURO.0390-17.2018

Cunningham, C.C., C.R. Malloy, and G.K. Radda. 1986. Effect of fasting and acute ethanol administration on the energy state of in vivo liver as measured by 31p-NMR spectroscopy. *Biochim. Biophys. Acta*. 885:12–22. https://doi.org/10.1016/0167-4889(86)90033-9

Davies, K.M., C. Anselmi, I. Wittig, J.D. Faraldo-Gómez, and W. Kühlbrandt. 2012. Structure of the yeast F1Fo-ATP synthase dimer and its role in shaping the mitochondrial cristae. *Proc. Natl. Acad. Sci. USA*. 109:13602–13607. https://doi.org/10.1073/pnas.1204593109

De Pinto, V., O. Ludwig, J. Krause, R. Benz, and F. Palmieri. 1987. Porin pores of mitochondrial outer membranes from high and low eukaryotic cells: Biochemical and biophysical characterization. *Biochim. Biophys. Acta*. 894:109–119. https://doi.org/10.1016/0005-2728(87)90180-0

Duyckaerts, C., C.M. Sluse-Goffart, J.P. Fux, F.E. Sluse, and C. Lièbecq. 1980. Kinetic mechanism of the exchanges catalysed by the adenine-nucleotide carrier. *Eur. J. Biochem*. 106:1–6. https://doi.org/10.1111/j.1432-1033.1980.tb05990.x

Garcia, G.C., T.M. Bartol, S. Phan, E.A. Bushong, G. Perkins, T.J. Sejnowski, M.H. Ellisman, and A. Skupin. 2019. Mitochondrial morphology provides a mechanism for energy buffering at synapses. *Sci. Rep*. 9:18306. https://doi.org/10.1038/s41598-019-54159-1

Glavis-Bloom, C., C.R. Vanderlip, S. Weiser Novak, M. Kuwajima, L. Kirk, K.M. Harris, U. Manor, and J.H. Reynolds. 2023. Violation of the ultrastructural size principle in the dorsolateral prefrontal cortex underlies working memory impairment in the aged common marmoset (Callithrix jacchus). *Front. Aging Neurosci*. 15:1146245. https://doi.org/10.3389/fnagi.2023.1146245

Gnaiger, E.; MitoEAGLE Task Group. 2020. Mitochondrial physiology. *Bioenerg. Commun*. 1. https://doi.org/10.26124/bec:2020-0001.v1

Gropp, T., N. Brustovetsky, M. Klingenberg, V. Müller, K. Fendler, and E. Bamberg. 1999. Kinetics of electrogenic transport by the ADP/ATP carrier. *Biophys. J*. 77:714–726. https://doi.org/10.1016/S0006-3495(99)76926-2

Heiske, M., T. Letellier, and E. Klipp. 2017. Comprehensive mathematical model of oxidative phosphorylation valid for physiological and pathological conditions. *FEBS J*. 284:2802–2828. https://doi.org/10.1111/febs.14151

Hill, T.L. 1989. Free Energy Transduction and Biochemical Cycle Kinetics. Academic Press. New York, https://doi.org/10.1007/978-1-4612-3558-3

Holmuhamedov, E.L., S. Jovanović, P.P. Dzeja, A. Jovanović, and A. Terzic. 1998. Mitochondrial ATP-sensitive K+ channels modulate cardiac mitochondrial function. *Am. J. Physiol*. 275:H1567–H1576. https://doi.org/10.1152/ajpheart.1998.275.5.H1567

Husar, A., M. Ordyan, G.C. Garcia, J.G. Yancey, A.S. Saglam, J. Faeder, T.M. Bartol Jr, and T.J. Sejnowski. 2022. Mcell4 with bionetgen: A Monte Carlo simulator of rule-based reaction-diffusion systems with python interface. *bioRxiv*. https://doi.org/10.1101/2022.05.17.492333 (Preprint posted May 19 2022)

Kaim, G., and P. Dimroth. 1999. ATP synthesis by F-type ATP synthase is obligatorily dependent on the transmembrane voltage. *EMBO J*. 18:4118–4127. https://doi.org/10.1093/emboj/18.15.4118

Keener, J.P., and J. Sneyd. 1998. Mathematical Physiology. Vol. 1. Springer. New York, https://doi.org/10.1007/b98841

Kerr, R.A., T.M. Bartol, B. Kaminsky, M. Dittrich, J.-C.J. Chang, S.B. Baden, T.J. Sejnowski, and J.R. Stiles. 2008. Fast Monte Carlo simulation methods for biological reaction-diffusion systems in solution and on surfaces. *SIAM J. Sci. Comput*. 30:3126–3149. https://doi.org/10.1137/070692017

Ko, Y.H., M. Delannoy, J. Hullihen, W. Chiu, and P.L. Pedersen. 2003. Mitochondrial ATP synthasome. Cristae-enriched membranes and a multiwell detergent screening assay yield dispersed single complexes containing the ATP synthase and carriers for Pi and ADP/ATP. *J. Biol. Chem*. 278:12305–12309. https://doi.org/10.1074/jbc.C200703200

Krämer, R., and M. Klingenberg. 1982. Electrophoretic control of reconstituted adenine nucleotide translocation. *Biochemistry*. 21:1082–1089. https://doi.org/10.1021/bi00534a040

Laguens, R. 1971. Morphometric study of myocardial mitochondria in the rat. *J. Cell Biol*. 48:673–676. https://doi.org/10.1083/jcb.48.3.673

Leung, A., D. Ohadi, G. Pekkurnaz, and P. Rangamani. 2021. Systems modeling predicts that mitochondria ER contact sites regulate the postsynaptic energy landscape. *NPJ Syst. Biol. Appl*. 7:26. https://doi.org/10.1038/s41540-021-00185-7

Livingston, B.E., R.A. Altschuld, and C.M. Hohl. 1996. Metabolic compartmentalization in neonatal swine myocytes. *Pediatr. Res*. 40:59–65. https://doi.org/10.1203/00006450-199607000-00011

Magnus, G. 1995. A Mitochondria-Based Model for Bursting and its D-Glucose Dependence in the Pancreatic Beta Cell. University of California, Davis, CA.

Magnus, G., and J. Keizer. 1997. Minimal model of beta-cell mitochondrial Ca2+ handling. *Am. J. Physiol*. 273:C717–C733. https://doi.org/10.1152/ajpcell.1997.273.2.C717

Mendelsohn, R., G.C. Garcia, T.M. Bartol, C.T. Lee, P. Khandelwal, E. Liu, D.J. Spencer, A. Husar, E.A. Bushong, S. Phan, et al. 2021. Morphological principles of neuronal mitochondria. *J. Comp. Neurol*. 530:886–902. https://doi.org/10.1002/cne.25254

Metelkin, E., I. Goryanin, and O. Demin. 2006. Mathematical modeling of mitochondrial adenine nucleotide translocase. *Biophys. J*. 90:423–432. https://doi.org/10.1529/biophysj.105.061986

Mörikofer-Zwez, S., and P. Walter. 1989. Binding of ADP to rat liver cytosolic proteins and its influence on the ratio of free ATP/free ADP. *Biochem. J*. 259:117–124. https://doi.org/10.1042/bj2590117

Nguyen, M.-H.T., S.J. Dudycha, and M.S. Jafri. 2007. Effect of Ca2+ on cardiac mitochondrial energy production is modulated by Na+ and H+ dynamics. *Am. J. Physiol. Cell Physiol*. 292:C2004–C2020. https://doi.org/10.1152/ajpcell.00271.2006

Nicholls, D.G. 2013. Bioenergetics. Fourth edition. Elsevier Science Amsterdam.

Nosek, M.T., D.T. Dransfield, and J.R. Aprille. 1990. Calcium stimulates ATP-Mg/Pi carrier activity in rat liver mitochondria. *J. Biol. Chem*. 265:8444–8450. https://doi.org/10.1016/S0021-9258(19)38908-2

Perkins, G., J.H. Lee, S. Park, M. Kang, M.C. Perez-Flores, S. Ju, G. Phillips, A. Lysakowski, M.A. Gratton, and E.N. Yamoah. 2020. Altered outer hair cell mitochondrial and subsurface cisternae connectomics are candidate mechanisms for hearing loss in mice. *J. Neurosci*. 40:8556–8572. https://doi.org/10.1523/JNEUROSCI.2901-19.2020

Pietrobon, D., and S.R. Caplan. 1985. Flow-force relationships for a six-state proton pump model: Intrinsic uncoupling, kinetic equivalence of input and output forces, and domain of approximate linearity. *Biochemistry*. 24:5764–5776. https://doi.org/10.1021/bi00342a012

Rulfs, J., and J.R. Aprille. 1982. Adenine nucleotide pool size, adenine nucleotide translocase activity, and respiratory activity in newborn rabbit liver mitochondria. *Biochim. Biophys. Acta*. 681:300–304. https://doi.org/10.1016/0005-2728(82)90035-4

Siegmund, S.E., R. Grassucci, S.D. Carter, E. Barca, Z.J. Farino, M. Juanola-Falgarona, P. Zhang, K. Tanji, M. Hirano, E.A. Schon, et al. 2018. Three-dimensional analysis of mitochondrial crista ultrastructure in a patient with leigh syndrome by in situ cryoelectron tomography. *iScience*. 6:83–91. https://doi.org/10.1016/j.isci.2018.07.014

Stiles, J.R., D. Van Helden, T.M. Bartol Jr, E.E. Salpeter, and M.M. Salpeter. 1996. Miniature endplate current rise times less than 100 microseconds from improved dual recordings can be modeled with passive acetylcholine diffusion from a synaptic vesicle. *Proc. Natl. Acad. Sci. USA*. 93:5747–5752. https://doi.org/10.1073/pnas.93.12.5747

Strauss, M., G. Hofhaus, R.R. Schröder, and W. Kühlbrandt. 2008. Dimer ribbons of ATP synthase shape the inner mitochondrial membrane. *EMBO J*. 27:1154–1160. https://doi.org/10.1038/emboj.2008.35

Tischler, M.E., P. Hecht, and J.R. Williamson. 1977. Determination of mitochondrial/cytosolic metabolite gradients in isolated rat liver cells by cell disruption. *Arch. Biochem. Biophys*. 181:278–293. https://doi.org/10.1016/0003-9861(77)90506-9

Vogel, F., C. Bornhövd, W. Neupert, and A.S. Reichert. 2006. Dynamic subcompartmentalization of the mitochondrial inner membrane. *J. Cell Biol*. 175:237–247. https://doi.org/10.1083/jcb.200605138

Wescott, A.P., J.P.Y. Kao, W.J. Lederer, and L. Boyman. 2019. Voltage-energized calcium-sensitive ATP production by mitochondria. *Nat. Metabol*. 1:975–984. https://doi.org/10.1038/s42255-019-0126-8

Wittig, I., and H. Schägger. 2009. Supramolecular organization of ATP synthase and respiratory chain in mitochondrial membranes. *Biochim. Biophys. Acta*. 1787:672–680. https://doi.org/10.1016/j.bbabio.2008.12.016

Yoshida, M., E. Muneyuki, and T. Hisabori. 2001. ATP synthase: A marvellous rotary engine of the cell. *Nat. Rev. Mol. Cell Biol*. 2:669–677. https://doi.org/10.1038/35089509

Supplemental material

ATP/ADP translocator: Experimental results

The ATP/ADP translocator model is based on the work of Metelkin et al. (2006), and two additional states were added to track futile translocation in the spatial model. Starting with steady-state flux parameters from Metelkin et al. (2006) for ANTs from heart mitochondria (Krämer and Klingenberg, 1982), we first estimated the parameters for the spatial implementation and the corresponding ODE model. To adapt the model to the non-steady-state condition, the backward and forward rate constants were estimated from the dissociation constants. The forward rate constants were set smaller than the diffusion-limited rate and the backward rate constants were set to satisfy the dissociation constant ratio. For instance, the dissociation constants at a membrane potential of 180 mV were $KTi \approx 400$ μM in the original paper, and in our simulations 500 μM was chosen. Similarly, K_{Di} was modified from 51 μM in the original paper to 25 μM in our simulations. We also estimated the dissociation constants from the matrix side K_{Tm} and K_{Dm} as 6.25 and 10 mM, respectively (the ratio is ≈1). With these modifications, we were able to qualitatively reproduce the independent data from Krämer and Klingenberg, (1982) and Duyckaerts et al. (1980) (Figs. S1 and S2).

We also qualitatively reproduced the experimental data of Duyckaerts et al. (1980), which proposed a mechanism for the ANT translocator which implies the formation of a ternary complex and proposed the explicit form for the flux as

$$v_o^{-1} = \frac{K_{AB}}{V} \frac{1}{[A][B]} + \frac{1}{V}. \quad (41)$$

From this relation, it follows that the reciprocal of the initial rate of exchange as a function of the concentrations of ADP in the matrix and outside should be linear as shown by the straight line in Fig. S2 E. From this relation, they also estimated the parameters from their data and obtained a value for K_{AB} of 26.5×10^{-3} mM^2. This value is in good agreement with our simulations, which gives a parameter value K_{AB} of 27.06×10^{-3} mM^2 (Fig. S2 F).

ATP/ADP translocator: comparison with other models

We compare the ANT model with another model in the literature. With the ANT model implemented by Magnus and Keizer (1997), developed by Bohnensack (1982), we analyzed how the ANT flux depends on the ATP_m/ADP_m ratio, and on the ATP_i/ADP_i (Fig. S3). Similar dependencies were shown in the main text for the ANT model implemented in this paper (Fig. S4, A and B).

Spatial simulations

Same number of ATP synthases in all the reconstructions. We performed spatial simulation with the same conditions considered in the main text, but kept the number of ATP synthases constant in all reconstructions (Fig. S4). The first five reconstructions are in the globular set and the last four are in the elongated one. On average, the globular set generates a rate of 17 ATPs/ms and the elongated one at a rate of 10 ATPs/ms; the difference is statistically significant (P value $<1.8 \times 10^{-6}$).

Comparison to our previous version of the model

We compare the dynamics of our previous version of the model (Garcia et al., 2019) and the current version for the mitochondrial reconstruction number 1 (Fig. S5). The ATP production rate with the new parameters of the model is 34 ± 2 ATPs/ms, whereas with the previous version the rate was 68 ± 2 ATPs/ms for the same reconstruction.
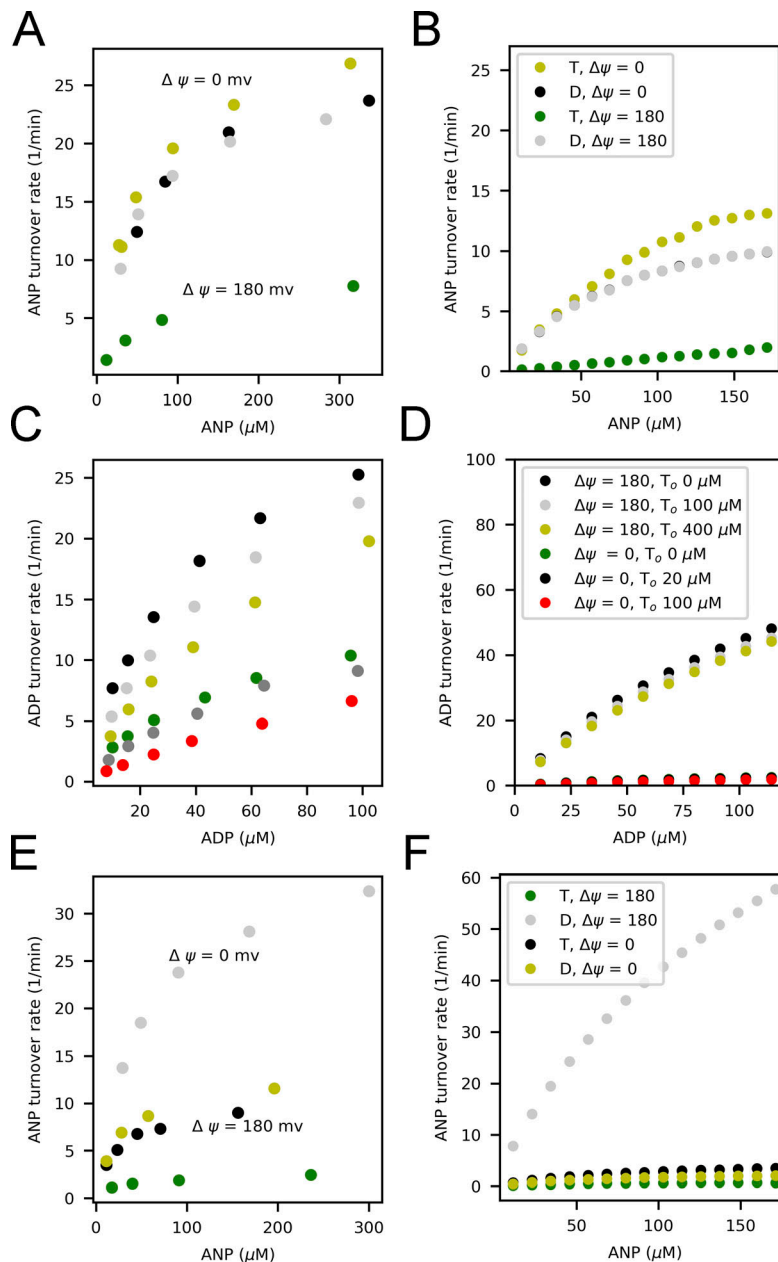
Figure S1. **Qualitative reproduction of experimental fluxes from published work (**Krämer and Klingenberg, 1982**). (A and B)** ATP uptake rate vs. external ATP concentration for a membrane potential (ΔΨ) of 0 and 180 mV in yellow and green, respectively. Black and grey points describe the ADP uptake rate vs. external ADP concentration for a membrane potential of 0 and 180 mV. **(A and B)** Transformed data from Krämer and Klingenberg (1982) (A; we followed the same approach as in Metelkin et al. [2006]), and our simulations (B), the flux was computed calculating an average over 30 s. ANP stands for ATP for the yellow and green points, and for ADP for black and grey points. **(C and D)** ADP uptake rate vs. external ADP concentration for membrane potential (ΔΨ) of 180 mV and ATP concentrations outside the liposomes (T_o) of 0, 100, 400 μM shown in black, light grey, and yellow points, respectively. Green, grey, and red points describe the dependency with the membrane potential of 0 mV and concentrations of ATP concentrations outside the liposomes (T_o) of 0, 20, 100 μM, respectively. The concentrations of ADP and ATP inside the liposomes were 5 mM. **(E)** ATP uptake rate vs. ATP concentration, yellow and green points for a membrane potential (ΔΨ) of 0 and 180 mV, respectively, and ADP concentration equal to the ATP concentration. **(F)** ADP uptake rate vs. ADP concentration, black and grey points for a membrane potential of 0 and 180 mV, respectively, and ATP concentration equal to the ADP concentration.
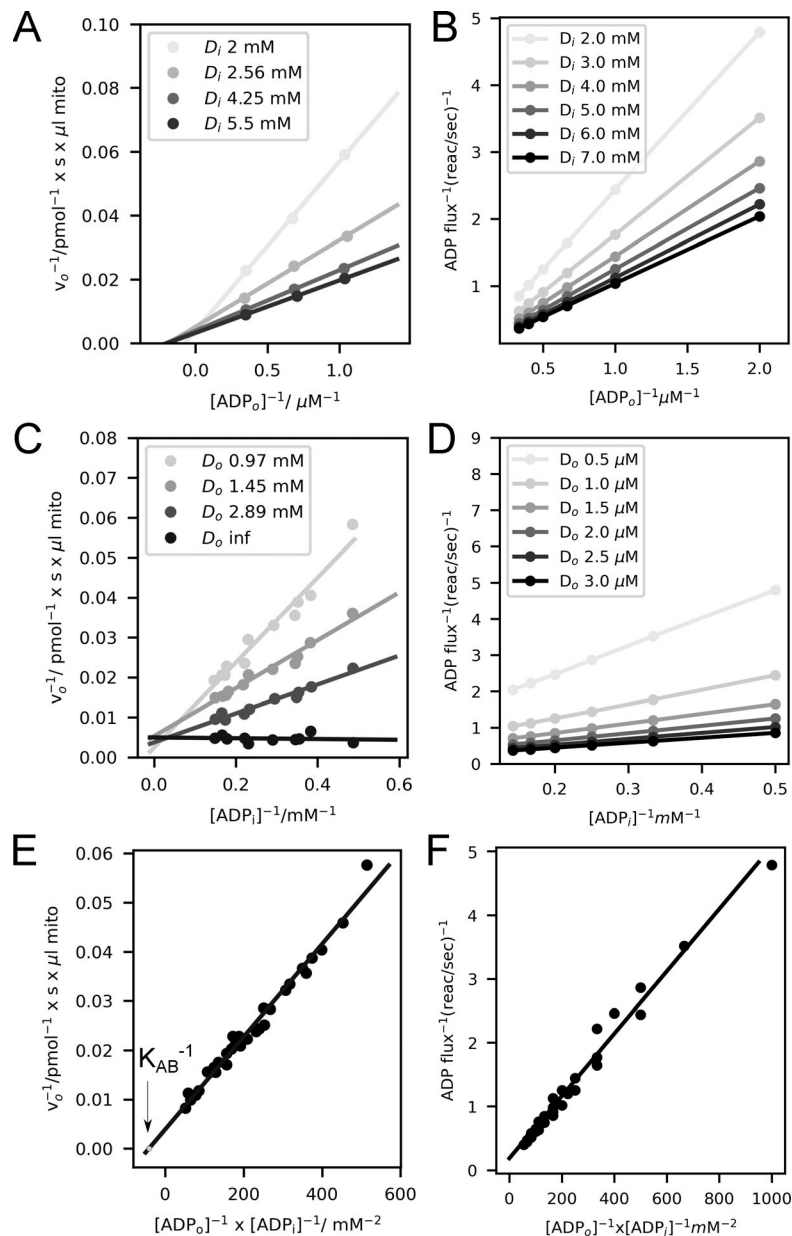
Garcia et al.
Mitochondrial morphology governs ATP production rate

Journal of General Physiology   S2
https://doi.org/10.1085/jgp.202213263

Figure S2. **Qualitative reproduction of the experimental results from published work (**Duyckaerts et al., 1980**). (A and B)** Reciprocal of the initial rate of ADP exchange as a function of the reciprocal of the external ADP concentration. The initial rate was measured for 3 external-ADP concentrations and 11 internal-ADP concentrations (only four are shown). The lines were calculated by the method of least squares. Experimental data reproduced from (A) Duyckaerts et al. (1980) and (B) our simulations. **(C and D)** Reciprocal of the initial rate of ADP exchange as a function of the reciprocal of the internal-ADP concentration. The initial rate was measured for 3 external ADP concentrations and 11 internal-ADP concentrations. Data reproduced from (C) Duyckaerts et al. (1980) and (D) our simulations. **(E and F)** Reciprocal of the initial rate of ADP exchange as a function of the reciprocal of $[ADP]_i[ADP]_o$. Data reproduced from (E) Duyckaerts et al. (1980), the parameter value K_{AB} is 26.5×10^{-3} mM^2, and (F) our simulations; our estimation of K_{AB} from our simulations is 27.06×10^{-3} mM^2.
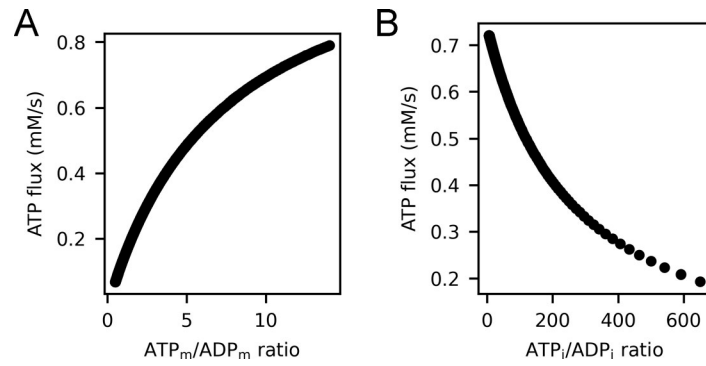
Figure S3. **Comparison with ANT model developed by** Bohnensack (1982)**. (A)** ATP flux dependence on the ATP to ADP ratio on the matrix. **(B)** ATP flux dependence on the ATP to ADP ratio in the IMS at a constant membrane potential of 180 mV.
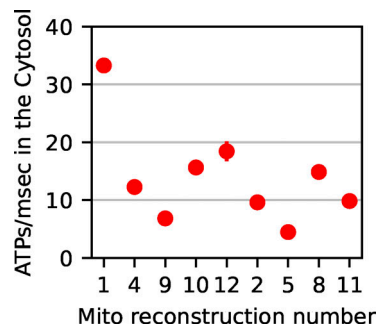

Figure S4. **ATP production rate in the cytosol for all reconstructions, considering the same number of ATP synthases (204).** The first five reconstructions belong to the globular set and the last four to the elongated one. On average the ATP production rate is also higher for the globular set under these conditions.
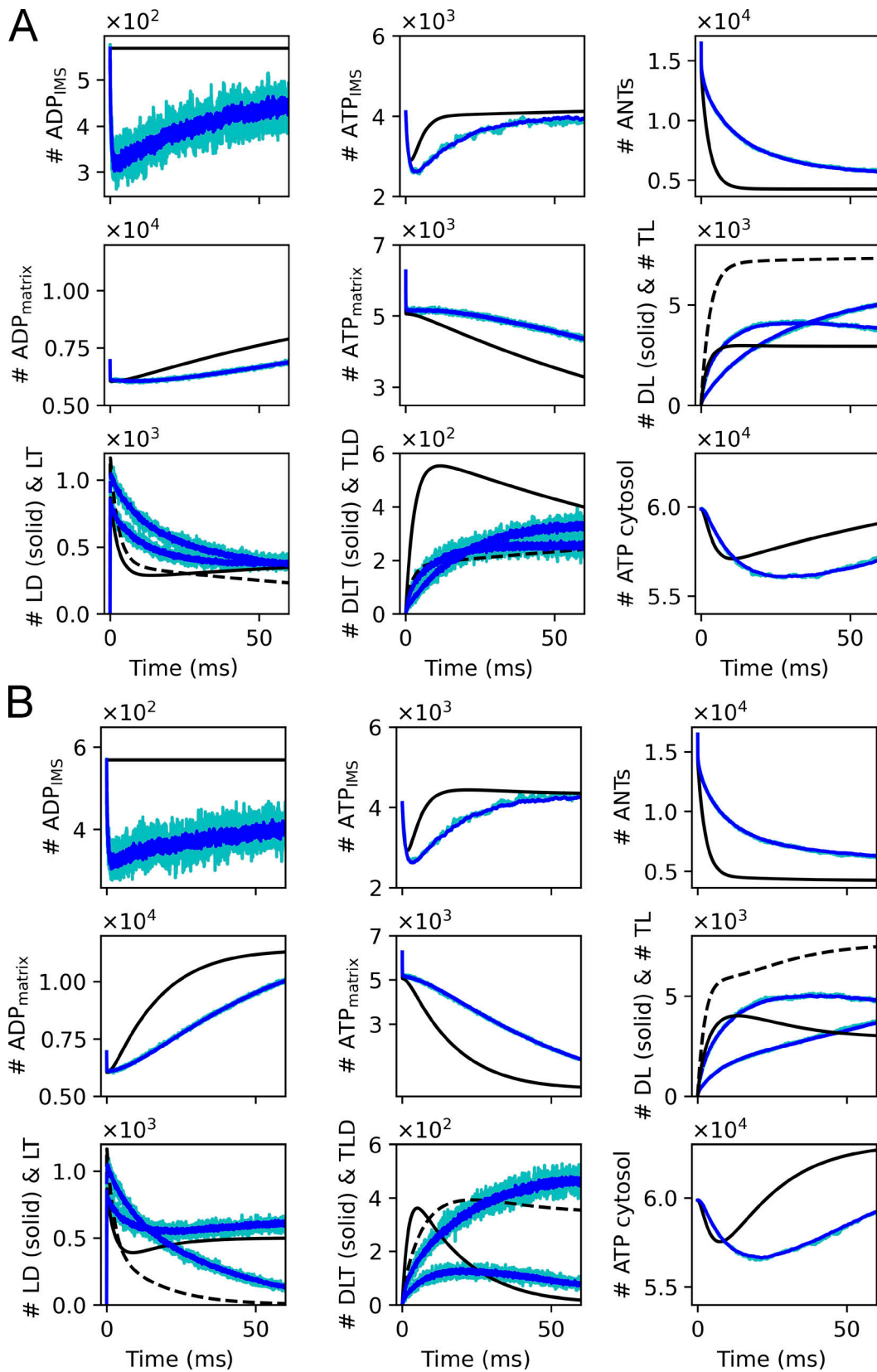
Figure S5. Comparison to our already-published model (Garcia et al., 2019). (A and B) Average traces of the number of molecules in the different compartments (in blue), a single trace (in cyan), and results of the ODEs (in black) on the left (A), results of our current version of the model and on the right (B) results for the same conditions for the old version of the model (Garcia et al., 2019), for reconstruction #1.